

CZECH TECHNICAL UNIVERSITY IN PRAGUE  
FACULTY OF NUCLEAR SCIENCES AND  
PHYSICAL ENGINEERING  
DEPARTMENT OF PHYSICS



## Research Report

### Measurement and Analysis of Magnetic Fields of the Tokamak GOLEM

Author: Bc. Tomáš Markovič

Supervisor: Ing. Ivan Ďuran, Ph.D.

Prague, 2011

**Title:** Measurement and Analysis of Magnetic Fields of the Tokamak GOLEM

**Author:** Bc. Tomáš Markovič

**Abstract:**

MHD activity of tokamak GOLEM during different operational regimes and experimental sessions is investigated. Upon overview and characterisation of manifestation and cause of basic tokamak MHD instabilities, engineering aspects of tokamak GOLEM that are relevant for MHD analysis are stated. This yields approximately doubled  $q$  magnitudes across the whole radial profile, compared to tokamak CASTOR and thus limitation of contained analysis to higher  $m$  islands. Additionally, magnetic fields and means of their measurement are summarized (and calibrated), with respective thumb rules of their magnitude stated. Generally this yields  $B_T \sim (5 \cdot) 10^2$  mT,  $B_\theta \sim 10^1$  mT and  $B_r \sim 10^0$  mT. Biot-Savart's law based model of poloidal  $B_T$  profile is compared to  $1/R$  dependence and to experimental data, yielding that by construction, GOLEM is tokamak of zero toroidal field ripple. Upon discussion on limitation of current means of magnetic diagnostics, construction of new set of sensors (containing set of extended temperature operational range Hall probes) is introduced. Following analysis of shot database by both basic parameter evolutions and use of statistical methods of Fourier transformation and cross-correlation on MHD instabilities data suggests tendency of plasma column to shift towards LFS and top of the chamber. Shift from HFS towards LFS is shown to reverse upon application of  $B_V$  field of horizontal position stabilisation. As shift towards top persists across all of the analysed discharges, it is recommended to apply field of vertical position stabilisation  $B_H$  as well. Cross-correlation analysis on MHD instabilities data by fast DAS implies emergence of Mirnov instabilities during initial current rise period, which suggests plasma edge rotation velocity to be in range of 6.28 – 31.42 km/s (depending on  $m$  number of observed structures).

**Key Words:** MHD instabilities, plasma disruption, cross-correlation, Tokamak GOLEM, toroidal field ripple, plasma rotation, magnetic diagnostics, plasma position estimation.

# Chapter 1

## Introduction

It is a well known fact that sudden plasma disruptions pose serious threat to successful tokamak operation. According to literature [1] (among many), main cause of disruption onset on tokamaks is due to magnetohydrodynamic (MHD) instabilities. Additionally, ref. [2] aims on disruption cause analysis of tokamak JET and identifies three principal classes of disruption causes i.e. density limit, low  $q$  operation and too rapid current rise, of which all three are associated with strong MHD instabilities. Since most of GOLEM discharges are terminated by sudden loss in confinement, aim of this paper is to investigate MHD activity of plasma in this tokamak. Analysis was mainly carried out by means of magnetic diagnostics and application of statistical methods. Naturally, complex analysis would require use of other means of plasma diagnostics as well – ref. [3] notes, that quantitative comparison of MHD instabilities experimental data obtained by magnetic diagnostics to theory would be challenging due to character of used methods. Namely, due to inability of magnetic field sensors to measure inner structure of observed instabilities. Nevertheless, many useful information on crucial MHD instabilities are provided by measurement of magnetic field perturbations at the plasma edge, as it is investigated (also) in this report.

Following chapter will provide a brief analytical introduction into characters of manifestation and cause of tokamak MHD instabilities. Chapters on plasma and magnetic field properties of tokamak GOLEM and available means of present and future magnetic diagnostics on this tokamak follow. After an actual analysis of different GOLEM discharges, the most important findings are summarized.

# Chapter 2

## MHD Instabilities of Tokamaks

Although plasma in tokamaks is subject to wide range of instabilities which are yet to be fully understood, literature [4] states that they can be from the most part assigned to MHD modes, as well as states two main causes for MHD instability onset – current and pressure gradients (the latter combined with adverse magnetic field curvature). Since scope of this report covers plasma of tokamak GOLEM, only instabilities which are present on short-pulsed small tokamaks of circular cross section and limiter configuration are analyzed. As their name suggests, the basic theoretical tool for characterisation of these instabilities is set of MHD equations [5]:

$$\frac{\partial \rho}{\partial t} + \nabla \cdot (\rho \mathbf{u}) = 0, \quad (2.1)$$

$$\frac{\partial \rho \mathbf{u}}{\partial t} + \nabla \cdot \left( p \mathbb{I} + \rho \mathbf{u} \otimes \mathbf{u} + \frac{B^2}{2\mu_0} \mathbb{I} - \frac{1}{\mu_0} \mathbf{B} \otimes \mathbf{B} \right) = 0, \quad (2.2)$$

$$\frac{\partial \mathbf{B}}{\partial t} = \frac{1}{\sigma \mu_0} \nabla^2 \mathbf{B} + \nabla \times (\mathbf{u} \times \mathbf{B}), \quad (2.3)$$

$$\frac{\partial}{\partial t} \left( \frac{\rho u^2}{2} + \frac{B^2}{2\mu_0} + e \right) + \nabla \cdot \left( \frac{\rho u^2}{2} \mathbf{u} + e \mathbf{u} + \mathbb{P} \cdot \mathbf{u} + \frac{1}{\mu_0} \mathbf{E} \times \mathbf{B} + \mathbf{q} \right) = 0, \quad (2.4)$$

$$e = \frac{p}{\gamma - 1}; \quad \mathbf{q} = -\kappa \nabla T; \quad \mathbf{E} = -\mathbf{u} \times \mathbf{B} + \frac{\nabla \times \mathbf{B}}{\sigma \mu_0}. \quad (2.5)$$

This set takes two different forms, depending on whether  $\sigma \rightarrow \infty$  or not. In the former case, the set of equations (and resultant instabilities) is referred to as ideal MHD, while the latter case is referred to as resistive MHD. In general, tokamak plasma has high  $\sigma$

and is thus described by ideal MHD equations (see [5]). As it will be shown in section 2.3, however small the  $\sigma$  term is over most of tokamak plasma, it plays crucial role in emergence of MHD instabilities.

## 2.1 Magnetic Islands

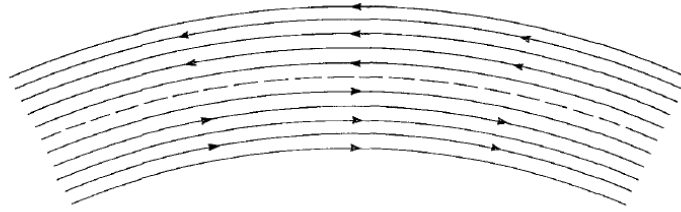


Figure 2.1: Sheared poloidal field in terms of  $B_\theta^*$  transformation [4].

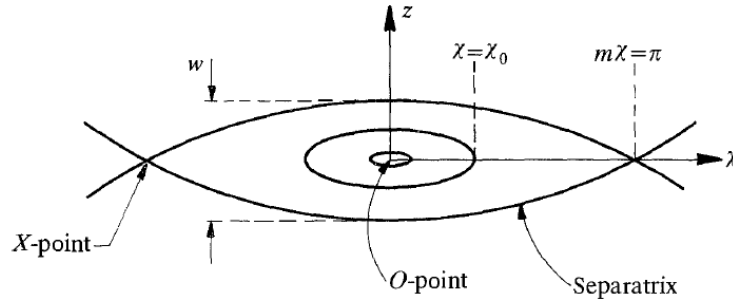


Figure 2.2: Characteristic local structure of perturbed  $B_\theta$  i.e. poloidal projection of magnetic island [4].

MHD instabilities in general tend to cause changes in magnetic topology. This change takes place on layers (or surfaces) of rational safety factor  $q$  and shape and width of resulting structures is straightforward to estimate [4]: Let  $q_s = \frac{m}{n}$  be the resonant surface in question with  $m$  being poloidal and  $n$  toroidal mode number of perturbations, whose poloidal plane projection takes form  $\sim \exp im\chi$ . Here  $\chi = \theta - \frac{n}{m}\phi$ . sought poloidal projection of perturbed field is inferred from equation of magnetic field line trajectory:

$$\frac{dr}{r_s d\chi} = \frac{B_r}{B_\theta^*} \quad (2.6)$$

where  $B_\theta^*$  is transformed sheared poloidal field in form

$$B_\theta^* = B_\theta \left(1 - \frac{n}{m} q(r)\right),$$

so that unperturbed  $B_\theta^*$  on rational surface is of zero magnitude and grows or decreases with respect to  $r$  coordinate, as can be seen in fig. 2.1. Radial width of perturbed topology structures tends to be initially small, thus first order Taylor around resonant surface is sufficient. This for unperturbed poloidal field yields

$$B_\theta^* = - \left( B_\theta \frac{q'}{q} \right)_{r_s} (r - r_s). \quad (2.7)$$

Magnetic field perturbation itself is of radial character in form

$$B_r(r, \chi) = \widehat{B}_r(r) \sin(m\chi). \quad (2.8)$$

By substitution of eq. 2.7 and eq. 2.8 into eq. 2.6 following expression is obtained:

$$-B_\theta \frac{q'}{q} (r - r_s) dr = r_s \widehat{B}_r \sin(m\chi) d\chi.$$

By assumption that quantities on the left hand side and  $\widehat{B}_r$  do not vary much in radial dimension over island width  $w$  and by substitution  $z = r - r_s$  (for more details see ref. [4]), resultant perturbed field line equation takes final form:

$$- \int_{r_s}^r (r' - r_s) dr' = \frac{r_s \widehat{B}_r q}{q' B_\theta} \int_{\chi_0}^{\chi} \sin(m\chi) d\chi',$$

$$z^2 = \frac{w^2}{8} (\cos(m\chi) - \cos(m\chi_0)) \quad \text{where} \quad w = 4 \left( \frac{r_s \widehat{B}_r q}{mq' B_\theta} \right)_{r_s}^{1/2}. \quad (2.9)$$

The respective perturbed magnetic surface structure can be seen in fig. 2.2. Such a structure of poloidal field can be detected and investigated either by poloidal array of Langmuir probes or by sensors of local magnetic field (preferably coils). Instability then presents itself as periodical oscillations of given spatial structure of measured signal, which is due to rotation of the islands.

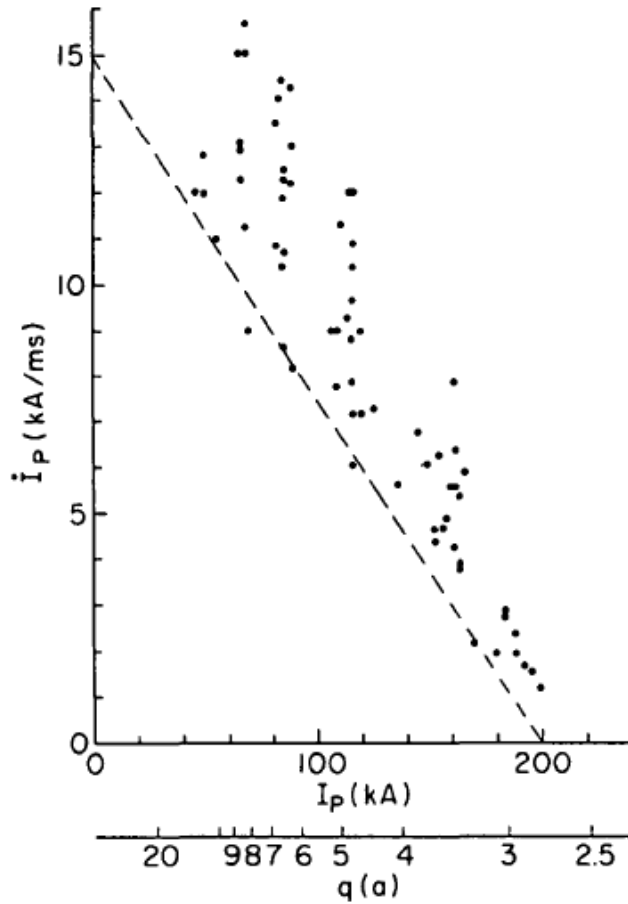


Figure 2.3: Emergence of current rise disruptions on Alcator A tokamak with dependance on global plasma parameters [6].

## 2.2 Disruptive MHD Instabilities

Growth of these islands to large amplitudes poses serious threat to plasma confinement as they break down the structure of nested magnetic surfaces. As one of the results, temperature profile is flattened across their width as investigated in ref.[3]. Moreover, interaction between islands of different rational  $q$  surfaces (or even the same, in hollow  $q$  profiles) can lead to complete breakdown of magnetic topology, resulting in ergodicity of magnetic field lines and massively enhanced particle transport [4]. According to classic theory approach, according to ref. [4] width of these islands grows nonlinearly until it reaches saturated value. This does not pose threat to plasma confinement, due to small size of saturated islands and mitigation of their further growth (see section 2.3.2). However, should a critical amount of energy be provided by some other phenomenon (such

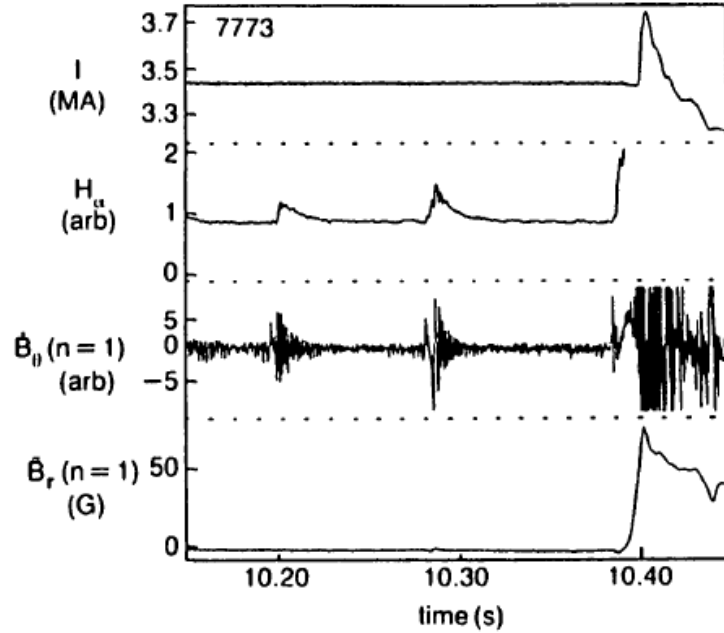


Figure 2.4: Low  $q$  disruption of shot no. 7773 on JET tokamak from the viewpoint of global tokamak parameters with sawteeth present [2].

as sawtooth instability onset), the island may grow into large amplitudes and result in disruption of confinement.

As was mentioned in the introduction, according to [2], the disruptions due to MHD activity can be divided into three categories. Current rise disruptions are associated with too rapid rise of  $I_p$  at the start-up resulting into hollow  $q$  profile (due to skin effect, i.e. finite rate of current penetration) and subsequent co-interaction of islands on the same resonant surfaces  $q_s$  nearby leads into ergodicity of magnetic field lines and transport enhancement. This kind of disruptions has been investigated in literature [6] on Alcator A tokamak. Major radius of 0.54 m, minor radius of 0.10 m and stainless bellows steel vacuum vessel of circular cross-section makes this tokamak very similar to GOLEM. Fig. 2.3, summarising disruptive situations for given global parameters of Alcator A suggests, that for current rise disruption are not expected to occur for discharge parameters of GOLEM (see section 3).

Disruptions due to low  $q$  are characterized by fast increase in  $n = 1$  instability (see ref. [2]), almost immediately followed by disruptive event itself, taking place without presence of any significant precursors. More theoretical insight into the problematics of

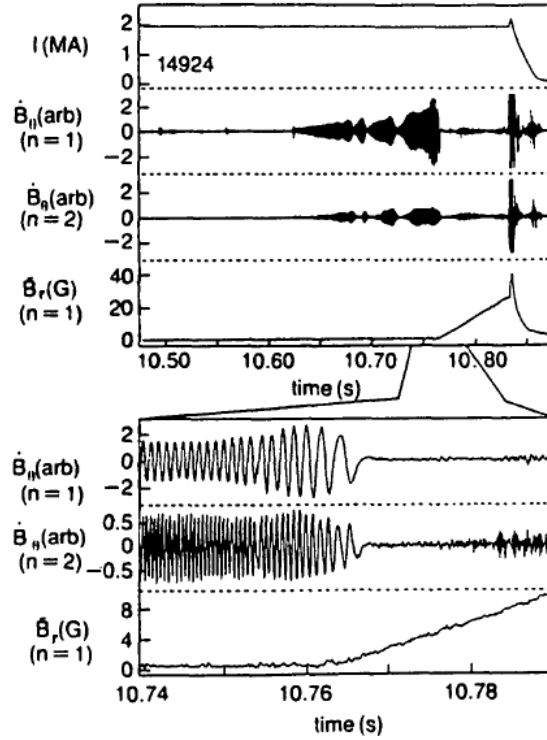


Figure 2.5: Idealized high density disruption of shot no. 14924 on JET tokamak from the viewpoint of global magnetic field parameters [2].

low  $q$  instabilities is provided in section 2.3.

On the other hand, disruptions caused by high density limit have more reliable and distinctive precursors. It is well established that generation, locking and subsequent growth to large amplitudes of  $m = 2$  island at the edge of plasma, is a reliable precursor to upcoming disruption – as can be seen in fig. 2.5. Island locking refers to decrease in its rotational frequency due to the plasma–conducting wall interaction, biased with an increase in amplitude of perturbation. Onset of this phenomenon is upon reach of sufficient amplitude of perturbation [2]. Even though situation in fig. 2.5 is very illustrative, standard form of high density limit MHD instabilities lies in series of small disruptions with increased MHD activity (growth of islands) followed by the main disruption event, as can be seen in fig. 2.6.

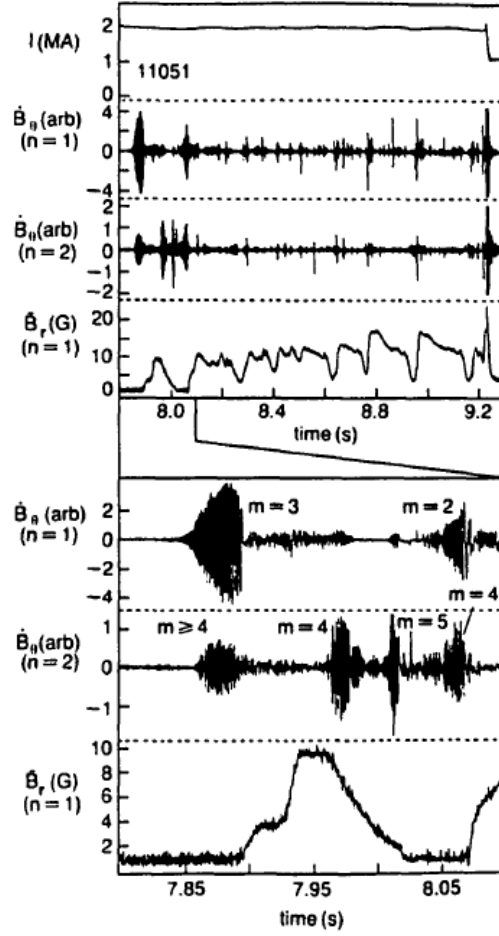


Figure 2.6: Standard high density disruption of shot no. 11051 on JET tokamak from the viewpoint of global magnetic field parameters [2].

## 2.3 Basic MHD Instabilities of Tokamak

Previous section summarized the behavior of MHD activity during disruptions and influence of instabilities on structure of magnetic surfaces. In order to provide insight into the cause of emergence of these islands, non-trivial theoretical analysis is necessary. With respect to different sets of basic equations being applied, the resultant instabilities are divided into two different classes, depending on whether the  $\sigma$  term of eq. 2.5 goes to infinity or not. The following two subsections are summarisation of a more detailed explanation from ref. [4].

### 2.3.1 Ideal MHD Instabilities

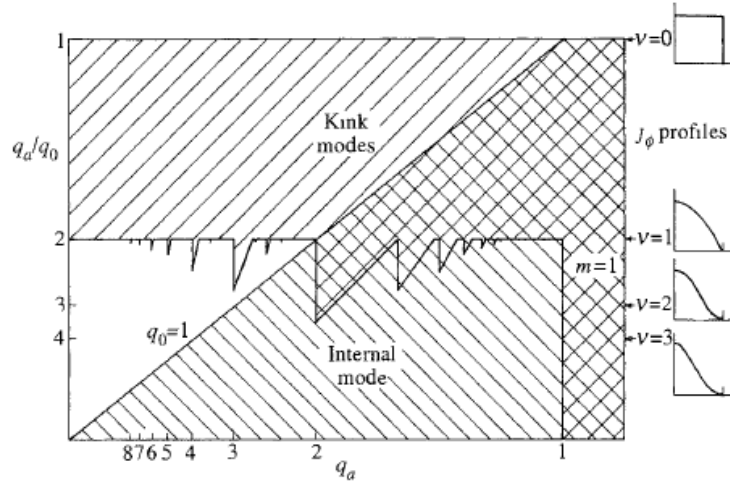


Figure 2.7: Combined stability diagram of constraints on  $q$  profile found in refs. [4] and [7].

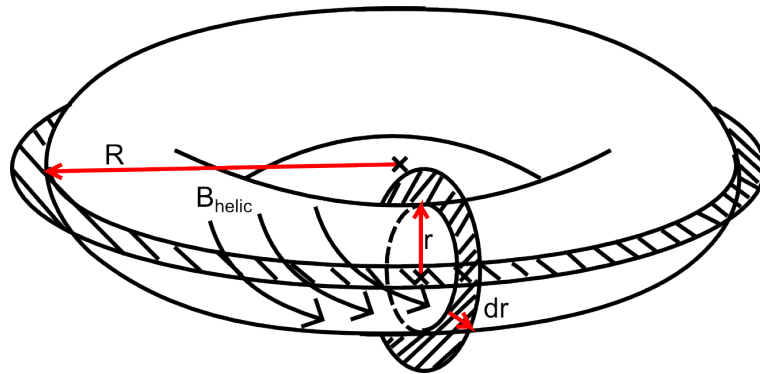


Figure 2.8: Geometry of  $q$  profile analysis for high aspect ratio tokamak of circular cross section.

Parameters of ideal MHD stability in tokamaks (i.e. so called region of stability) are primarily given by two similar criteria. The first criterion for kink stability gives constraints on character of  $q$  profile, while Kruskal-Shafranov stability criterion constraints on absolute minimal value for  $q$  over the whole plasma represent the second criterion. The conjunction of plausible  $q$  profiles and magnitudes can be seen in fig. 2.7.

To analyse the kink stability, maximum entropy approach is used. It is then straightforward to infer that instabilities represent tendencies of the system to lower its overall

energy. This approach is used to describe majority of tokamak instabilities (i.e. not only those of MHD character), and is referred to as energy principle. Its principal form is

$$\delta W = -\frac{1}{2} \int_V \boldsymbol{\xi} \cdot \mathbf{F} dV,$$

with  $\boldsymbol{\xi}$  being vector of displacement and  $\mathbf{F}$  force arising from displacement. Should this yield  $\delta W < 0$  for analysed situation, instability would develop. It should be noted on this place that most of the expressions provided below (concerning kink stability) can be found in literature [4] for further reference. By assumption of only linear terms:

$$\mathbf{F} = \mathbf{j}_1 \times \mathbf{B}_0 + \mathbf{j}_0 \times \mathbf{B}_1 - \nabla p_1. \quad (2.10)$$

With condition on conservation of entropy (i.e. adiabatic equation) and mass

$$p_1 = \gamma p_0 \nabla \cdot \boldsymbol{\xi} - \boldsymbol{\xi} \cdot \nabla p_0. \quad (2.11)$$

Linear form of Ampere's law yields

$$\mathbf{j}_1 = \frac{1}{\mu_0} \nabla \times \mathbf{B}_1, \quad (2.12)$$

and by substitution of eq. 2.11 - 2.12 into eq. 2.10, and this into fundamental relation of energy principle (with use of vector identities and by separating volume into two different regions due to different terms in each of them), it takes form

$$\delta W = \frac{1}{2} \int_{V_p} \left( \gamma p_0 (\nabla \cdot \boldsymbol{\xi})^2 + (\boldsymbol{\xi} \cdot \nabla p_0) \nabla \cdot \boldsymbol{\xi} + \frac{B_1^2}{\mu_0} - \mathbf{j}_0 \cdot (\mathbf{b}_1 \times \boldsymbol{\xi}) \right) dV + \int_{V_v} \frac{B_v^2}{2\mu_0} dV.$$

Here  $V_p$  (resp.  $V_v$ ) stands for volume of plasma (resp. vacuum) region and  $B_v$  for vacuum field. This approach is commonplace in analysis of MHD stability and similar calculation can be found also in literature [9]. In order to obtain relevant analytical expressions, large aspect ratio approximation is necessary. Also to further simplify the problem, cylindrical coordinate system (ref. [4] states that result does not differ significantly from toroidal case analysis) and plasma incompressibility of  $\nabla \cdot \boldsymbol{\xi} = 0$  (ref. [8] states that compressible plasma is rather stabilising) are assumed. After this transformation and by negligence of toroidal terms, expression for  $\delta W$  takes form

$$\delta W = \pi R \int_0^a \left( \frac{B_{r1}^2 + B_{\theta 1}^2}{\mu_0} - j_{z0} (B_{r1} \xi_\theta - B_{\theta 1} \xi_r) \right) r d\theta dr + \pi R \int_a^b \frac{B_v^2}{\mu_0} r d\theta dr. \quad (2.13)$$

Parameter  $a$  stands for plasma edge radius and  $b$  for liner radius (provided it is perfectly conducting). This implies that first integral in eq. 2.13 represents plasma region, with second integral representing vacuum region. It is evident that contribution of vacuum region has stabilising effect. The plasma contribution in obtained relation is not as straightforward to interpret as that of vacuum, and therefore this term will be analysed further: plasma incompressibility provides relation between  $\xi_r$  and  $\xi_\theta$ . Putting together Ohm's law for  $\sigma \rightarrow \infty$  and Faraday's equation, it is possible to express  $B_{r1}$  and  $B_{\theta1}$  in terms of  $\xi_r$  dependence. In literature [4], there is a calculation containing substitution of these past terms into eq. 2.13, integration per partes, modification and cancellation of some of the terms in order to obtain following expression for plasma contribution:

$$\begin{aligned} \delta W_p = & \frac{\pi^2 B_\phi^2}{\mu_0 R} \int_0^a \left[ \left( r \frac{d\xi}{dr} \right)^2 + (m^2 - 1) \xi^2 \right] \left( \frac{n}{m} - \frac{1}{q} \right) r dr \\ & + \left[ \frac{2}{q_a} \left( \frac{n}{m} - \frac{1}{q_a} \right) + \left( \frac{n}{m} - \frac{1}{q_a} \right)^2 \right] a^2 \xi_a^2. \end{aligned} \quad (2.14)$$

It needs to be noted that  $q(r) = \frac{r B_\phi}{R B_\theta}$  since large aspect ratio and circular cross section is assumed. From expression 2.14 it is evident that only one term can make  $\delta W_p$  negative (provided that  $m \geq 1$ ) i.e.  $\left( \frac{n}{m} - \frac{1}{q_a} \right)$  term. However, since  $q$  profile in tokamaks has usually increasing character, this would imply that tokamaks are ideally MHD stable. To obtain general instability source inside of plasma volume, an assumption of non-zero resistivity is necessary – see section 2.3.2.

Although eq. 2.14 stands in favor of general MHD stability of the whole plasma volume (as far as ideal MHD is concerned), ideal MHD instabilities do occur and in large scale at it. These instabilities are attributed to internal  $m = 1$   $n = 1$  modes and are onset of drop in central  $T_e$  (also of central  $q$  flattening) after previous gradual increase in this temperature. As this process repeats itself, the temporal evolution of  $T_e$  resembles sawteeth and is referred to as sawtooth instability. This process is yet to be fully understood, nevertheless the trigger of sawtooth relaxation process is experimentally well established to be violation of Kruskal-Shafranov criterion (see papers [10] and [11]). Vast experimental evidence enables to use this criterion on tokamaks, even though it is derived for cylindrical pinch. The full derivation of the criterion is provided (for example) in ref. [8] and thus only key expressions will be explicitly stated.

Let there be assumed a cylindrical plasma string with  $\mathbf{j}(\mathbf{r}) \neq 0$  only at the edge of plasma (i.e.  $r = a$ ). Once again it should be reminded, that in this paragraph, Kruskal-

Shafranov criterion is to be derived, whose use on tokamaks was justified by experiment and not by the way of its derivation, since used assumptions significantly differ from tokamak conditions. Let the main set of equations be eq. 2.1 – 2.5 for  $\sigma \rightarrow \infty$  with incompressible plasma of  $\nabla \cdot \xi$  and equilibrium field inside of plasma  $\mathbf{B}_0 = (0, 0, B_0)$  and in vacuum region  $\mathbf{B}'_0 = (0, B_\theta(r), B_z)$ . By considering first degree perturbations only (and by expressing  $\frac{\partial \xi}{\partial t} = \mathbf{u}_1(\mathbf{r}, t)$ ), equation for displacement vector is obtained in form:

$$\rho_0 \frac{\partial^2 \xi}{\partial t^2} = \mathbf{F}(\xi(\mathbf{r}, t)), \quad (2.15)$$

$$\begin{aligned} \mathbf{F}(\xi) = & \nabla(\xi \cdot \nabla p_0 + \gamma p_0 \nabla \cdot \xi) + \frac{1}{\mu_0} (\nabla \times \mathbf{B}_0) \times [\nabla \times (\xi \times \mathbf{B}_0)] \\ & + \frac{1}{\mu_0} ([\nabla \times \nabla \times (\xi \times \mathbf{B}_0)] \times \mathbf{B}_0). \end{aligned} \quad (2.16)$$

By further assumption that  $\xi(\mathbf{r}, t) = \xi(\mathbf{r}) \exp(i\omega t)$  and by implemetation of assumed plasma string into eq. 2.15 – 2.16, equation for  $\xi$  yields:

$$-\rho_0 \omega^2 \xi = \gamma p_0 \nabla(\nabla \cdot \xi) + \frac{1}{\mu_0} (\nabla \times \mathbf{B}_1) \times \mathbf{B}_0. \quad (2.17)$$

In previous equation, the fact that  $p_0 = \text{const}$  due to  $\mathbf{j}(r \neq a) = 0$  in equilibrium equation  $\mathbf{j} \times \mathbf{B} = \nabla p$  was used. Obtained set of equations will be solved separately for plasma and vacuum region, only for solutions to be put together at the end of calculation by boundary conditions:

$$[\mathbf{n} \cdot \mathbf{B}]_1^2 = 0, \quad (2.18)$$

and

$$[\mathbf{n} \times \mathbf{B}]_1^2 = \mu_0 \mathbf{j}. \quad (2.19)$$

Sought solution for diplacement vector will be of assumed to be of periodical form  $\xi(\mathbf{r}) = (\xi_r(r), \xi_\theta(r), \xi_z(r)) \exp(i(m\theta + kz))$ . By putting this, together with plasma incompressibility, into eq. 2.3, expression

$$\mathbf{B}_1 = ikB_0 \xi \quad (2.20)$$

is to be obtained. By substitution of this expression into eq. 2.17 and by application of divergence, the equation yields

$$\nabla^2 \xi_z = 0,$$

which in fact represents Bessel equation

$$\left[ \frac{d^2}{dr^2} + \frac{1}{r} \frac{d}{dr} - \left( k^2 + \frac{m^2}{r^2} \right) \right] \xi_z(r) = 0,$$

with solution

$$\xi_z(r) = \xi_z(a) \frac{I_m(kr)}{I_m(ka)}. \quad (2.21)$$

$I_m$  in 2.21 stands for modified Bessel function of first kind of  $m$  order (see appendix in ref. [5] for more information on Bessel functions). Radial component of displacement vector is obtained by substitution of obtained solution for z-component and eq. 2.20 into radial component of eq. 2.17. Its form is thus

$$\xi_r(r) = -\frac{ik^2 B_0^2 \xi_z(a)}{(k^2 B_0^2 - \mu_0 \rho \omega^2)} \frac{I'_m(kr)}{I_m(ka)}. \quad (2.22)$$

As for vacuum solution, thanks to absence of currents outside of plasma,  $\mathbf{B}'_1$  has zero curl which implies existence of potential  $\phi$  such that

$$\mathbf{B}'_1 = \nabla \phi,$$

while  $\phi(r, \theta, z) = \phi(r) \exp(i(m\theta + kz))$ . This is combined with trivial information that  $\nabla \cdot \mathbf{B}'_1 = 0$ , only to obtain the same equation for  $\phi$  as for  $\xi_z$ . Literature [8] here points out necessity to choose such a term in solution so that  $\phi(r) \rightarrow 0$  as  $r \rightarrow \infty$ . This yields

$$\phi(r) = \phi(a) \frac{K_m(kr)}{K_m(ka)}. \quad (2.23)$$

$K_m$  denotes modified Bessel functions of second kind of  $m$  order (once again, see ref. [5]). After obtaining solutions both in plasma and vacuum, substitution into boundary conditions 2.18 and 2.19 can take place. However before that, it will be necessary to expand all the quantities in following manner:

$$f(\mathbf{r}, t) \sim f_0(\mathbf{r}_0) + \xi \cdot \nabla f_0 + f_1(\mathbf{r}, t).$$

where  $\mathbf{r}_0$  denotes unperturbed boundary radius. By application of Gauss's theorem on equation of motion (momentum conservation equation, i.e. eq. 2.2) integrated over

cylinder whose length  $\rightarrow 0$  and with boundary in its center, there remains only one non-zero term, resulting in

$$\left[ p + \frac{B^2}{2\mu_0} \right]_1^2 = 0, \quad (2.24)$$

and is equivalent to eq. 2.18. By substitution of first-order terms of calculated variables into eq. 2.24 with environment 1 being plasma and 2 vacuum (or vice versa):

$$ikB_0^2\xi_z(a) = \left[ ikB_z + i\frac{m}{a}B_\theta(a) \right] \phi(a) - \frac{B_\theta^2(a)}{a} \xi_r(a). \quad (2.25)$$

As for eq. 2.19, provided that plasma is perfect conductor at whose edge normal component of magnetic field is not present, expression

$$\mathbf{B} \cdot \mathbf{n} = \mathbf{B}' \cdot \mathbf{n} = 0 \quad (2.26)$$

is valid at the same time at the border of plasma and vacuum volumes. By assuming vacuum region in eq. 2.26, first order quantities leave:

$$[\mathbf{B}'_1 + (\xi \cdot \nabla)\mathbf{B}'_0] \cdot \mathbf{n}_0 + \mathbf{B}'_0 \cdot \mathbf{n}_1 = 0. \quad (2.27)$$

It can be shown that  $\mathbf{n}_1 = -\nabla\xi_r$  and thus substitution of known quantities into eq. 2.27 gives

$$\left( \frac{d\phi}{dr} \right)_a - ikB_z\xi_r(a) - i\frac{m}{a}B_\theta(a)\xi_r(a) = 0. \quad (2.28)$$

Finally, is the sought dispersion relation obtained by substitution of found solutions for plasma (e.g. eq. 2.22) and vacuum (i.e. eq. 2.23), along with first boundary condition (i.e. eq. 2.25) into second boundary condition (i.e. eq. 2.28):

$$\frac{\omega^2}{k^2} = \frac{B_0^2}{\mu_0\rho} - \frac{(B_z + mB_\theta(a)/ka)^2}{\mu_0\rho} \frac{I'_m(ka)K_m(ka)}{I_m(ka)K'_m(ka)} - \frac{B_\theta^2(a)}{\mu_0\rho} \frac{I'_m(ka)}{kaI_m(ka)}. \quad (2.29)$$

Dispersion relation in itself is ratio of frequency of perturbation and its absolute spatial dimensions (i.e. wavelength), subjected to equations characterising environment where this perturbation might emerge. Having form of eq. 2.29,  $\omega$  can be either real or pure imaginary, which implies that in assumed plasma column located in vacuum, event. emerging periodical perturbations of plasma edge can either be rapidly stabilised or grow exponentially, depending on their relative size to column radius, plasma current and density and magnitude of stabilising field. However, obtained relation is still too complex to derive

any relevant analytical conclusions. Fortunately, for large perturbations such as kink instabilities, it is valid that  $|ka| \ll 1$ , which justifies the use of approximations

$$I_m(x) \approx \frac{(x/2)^m}{m!},$$

and

$$K_m \approx \frac{(m-1)!}{2} \left(\frac{x}{2}\right)^{-m}.$$

By substitution of these expressions into dispersion relation 2.29, much straightforward expression is obtained:

$$\mu_0 \rho \omega^2 = k^2 B_0^2 + \left[ k B_z + \frac{m}{a} B_\theta(a) \right]^2 - \frac{m}{a^2} B_\theta^2(a). \quad (2.30)$$

This expression can be simplified even further. By putting equilibrium pressure of plasma and vacuum into equivalence, i.e.

$$p_0 + \frac{B_0^2}{2\mu_0} = \frac{B_z^2}{2\mu_0} + \frac{B_\theta^2(a)}{2\mu_0},$$

and by substitution of this equivalence into eq. 2.30, along with  $m = 1$  (since this poloidal number is of interest when internal kink is in question) expression

$$\omega^2 = \frac{k_2 B_z^2}{\mu_0 \rho} \left[ 2 \left( 1 + \frac{B_\theta(a)}{ka B_z} \right) + \frac{B_\theta^2(a)}{B_z^2} - \beta_t \right]$$

is obtained ( $\beta_t = 2\mu_0 p_0 / B_z^2$  is equivalent to toroidal beta in tokamaks). With final assumption of  $\beta_t \ll 1$  and  $B_\theta(a)/B_z \ll 1$ , so that last and middle term are negligible compared to the first one, condition of stability is equivalent to  $|B_\theta(a)/B_z| < |ka|$ . As a byproduct of analysis, it was also shown that instabilities can grow (with respect to time) only into direction antiparallel to stabilising field (provided that axial vacuum field and stabilising field inside of plasma are parallel). Ref. [8] further explicitly states that  $|k|$  must be greater than  $2\pi/L$  where  $L$  stands for plasma column length (which for toroid stands for  $L = 2\pi R_0$ ). This finally gives the sought Kruskal-Shafranov stability criterion:

$$\frac{a B_z(a)}{R_0 B_\theta(a)} = q(a) > 1. \quad (2.31)$$

Let there be noted, that virtually the same analysis of plasma column stability, although without the derivation of Kruskal-Shafranov criterion, can be found also in ref. [5] among many. Even though the resultant relation in eq. 2.31 is bound to plasma edge, the criterion was shown to apply in

$$q(r) > 1 \quad \text{where} \quad 0 < r < a$$

fashion as well.

As for an actual form of  $q$  profile, in the case of large aspect ratio tokamak of circular cross section it is straightforward to derive. Application of one of the definitions by means of toroidal flux change to change in poloidal flux, namely

$$q = \frac{d\chi}{d\psi},$$

on tokamak of circular cross section yields

$$q(r) = \frac{2\pi r dr B_T}{2\pi R dr B_\theta(r)} = \frac{r}{R} \frac{B_T}{B_\theta(r)}. \quad (2.32)$$

By definition of  $q$ , Kruskal-Shafranov criterion can be physically interpreted as that plasma may be ideally MHD stable only when increment of dimensions of analysed plasma shape yields larger increment of magnetic flux due to enlargement of poloidal plane than increment of magnetic flux due to increased surface around the plasma (see surface increments in fig. 2.8). As relation 2.32 suggests, in the case of circular cross section tokamak of large aspect, this ratio of eventual flux increments is fully given by plasma shape ( $\frac{r}{R}$  component) and by helicity of overall magnetic field ( $\frac{B_T}{B_\theta(r)}$  component). It should be noted that  $R$  in previous relation represents major radius of the toroid only when large aspect ratio tokamak is assumed, so that  $R + r \approx R$  for every  $r$ .  $B_\theta$  can be expressed by means of current density  $j(r) = (1 - (r/a)^2)^\nu$  as

$$B_\theta(r, \nu) = \frac{\mu_0 j_0}{r} \int_0^r \rho \left(1 - \frac{\rho^2}{a^2}\right)^\nu d\rho.$$

where  $j_0$  represents current density in center of plasma column. This term can be expressed by means of total plasma current  $I_p$  by integration of current density up to limiter radius  $a$  and putting  $I(a, \nu) = I_p(\nu)$ , so that

$$j_0 = \frac{\nu + 1}{\pi a^2} I_p.$$

By substitution of previous two relations and trivial integration, final relation is for  $q$  profile is obtained in form

$$q(r, \nu) = \frac{2\pi B_T}{R\mu_0 I_p} \frac{r^2}{1 - \left(1 - \frac{r^2}{a^2}\right)^{\nu+1}}. \quad (2.33)$$

### 2.3.2 Resistive MHD Instabilities

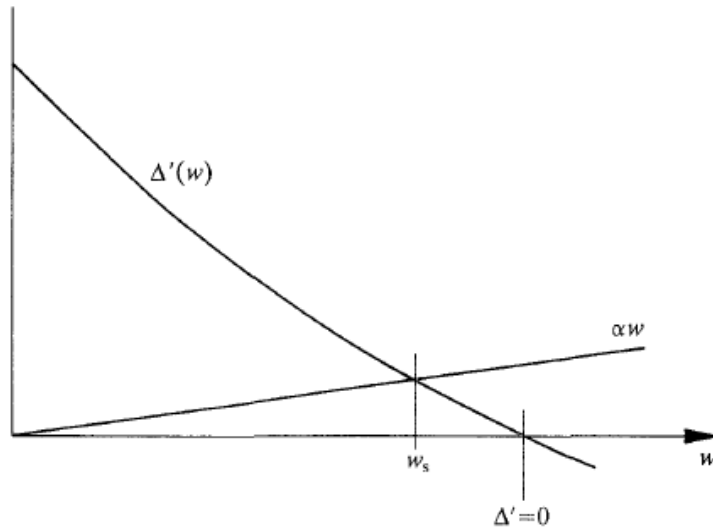


Figure 2.9: Evolutions of  $w$ -dependant terms of eq. 2.39 [4], implying stability of saturated width  $w_s$ .

Provided that Kruskal-Shafranov criterion is fulfilled for every  $r < a$  (i.e.  $q$  profile parameters lay in region of stability in fig. 2.7), section 2.3.1 implies that tokamak plasma should be then MHD stable. This however, is in contrary to standard experimental experience that tokamak is subject to MHD instabilities even when this criterion is not violated. This is due to the fact that tokamak plasma has non-zero resistivity (however small), which enables diffusive term of magnetic field equation to become significant on resonant surfaces of rational  $q$ , as contribution of magnetic field line freezing term goes to zero (see eqs. below). Diffusive term enables magnetic field energy to be transformed into plasma particle kinetic energy during reconnection of magnetic field lines. This process provides free energy for emergence and growth of instability and is yet to be fully understood (summarisation of current models of reconnection can be found in ref. [5]). As [8] notes, resistive instabilities were investigated for the first time in ref. [12]. Use of calculations stated therein would go far beyond scope of this report, nevertheless it was this publication where spontaneous resistive instabilities were referred to as tearing modes (due to the tearing and reconnection of magnetic field lines) for the first time

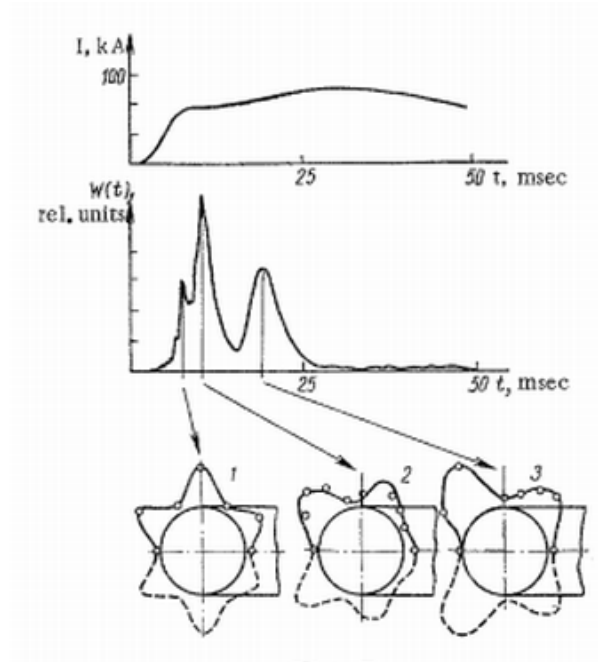


Figure 2.10: Relation of magnetic field oscillations to plasma current as observed in ref. [13]. Please note that  $w$  quantity here does not represent island width but magnitude of  $B_\theta$  perturbations (although these two quantities strongly correlate with each other).

and this name they retained until now. Since their onset is spontaneous, their influence on magnetic island width evolution will be shown, under assumption that emergence of these instabilities on resonant  $q$  surface already took place. For reference purposes, the following calculation can be also found in literature [4].

Taking curl of Ampere's law and by substitution of Faraday's law into this equation yields

$$\nabla \times \nabla \times \mathbf{B} = -\varepsilon_0 \mu_0 \frac{\partial^2 \mathbf{B}}{\partial t^2} + \mu_0 \sigma \left( \frac{\partial \mathbf{B}}{\partial t} + \nabla \times (\mathbf{u} \times \mathbf{B}) \right) \quad (2.34)$$

Into eq. 2.34, resistive Ohm's law in form of

$$\mathbf{j} = \sigma(\mathbf{E} + \mathbf{u} \times \mathbf{B})$$

has already been substituted. In literature [8] (among many) it is shown that in non-relativistic approximation, the first term on the right-hand side of eq. 2.34 may be neglected. Additionally, ref. [4] states that as far as vicinity of resonant magnetic surface

of rational  $q$  is concerned,  $\mathbf{u} \times \mathbf{B}$  term goes to zero. Thus, with use of trivial vector identity and that  $\nabla \cdot \mathbf{B} = 0$ , final form of resistive MHD equation for magnetic field is obtained in form

$$\frac{\partial \mathbf{B}}{\partial t} = \frac{1}{\mu_0 \sigma} \nabla^2 \mathbf{B}. \quad (2.35)$$

Previous expression represents magnetic field equation as used in resistive MHD in the case that freezing of magnetic field lines into plasma is negligible to their diffusion. It should be noted that over the most part of plasma volume, in tokamak plasmas freezing term of  $\mathbf{u} \times \mathbf{B}$  is dominating and it is diffusive term that tends to be negligible (see [5]). In eq. 2.35, the only  $\mathbf{B}$  component that is not constant on the magnetic island is the radial one, yielding

$$\frac{\partial B_r}{\partial t} = \frac{1}{\mu_0 \sigma} \frac{\partial^2 B_r}{\partial r^2}. \quad (2.36)$$

Evolution of magnetic island width  $w$  is obtained by substitution of eq. 2.9 into eq. 2.36 and by integration of obtained expression over the whole island width (provided  $B_r(r) \approx \text{const}$  over the island, though not the derivation):

$$\frac{dw}{dt} \approx \frac{1}{2\mu_0 \sigma B_r} \left[ \frac{\partial B_r}{\partial r} \right]_{r_s-w/2}^{r_s+w/2}.$$

It can be shown that  $B_r = -im\psi/r$ . Therefore

$$\frac{dw}{dt} \approx \frac{1}{2\mu_0 \sigma} \frac{\psi'}{\psi}. \quad (2.37)$$

Tearing instabilities are characterised by quantity of

$$\Delta'(w) = \left[ \frac{\psi'}{\psi} \right]_{r_s-w/2}^{r_s+w/2},$$

and thus final relation for growth of magnetic island is in form:

$$\frac{dw}{dt} \approx \frac{1}{2\mu_0 \sigma} \Delta'(w). \quad (2.38)$$

It is evident that this expression is only of approximate character. Nevertheless it is sufficient to provide insight into causes and assumptions of island growth due to resistive MHD. Relation of 2.38 is straightforward solution of magnetic field equation for toroidally symmetric resistive plasma of dominant  $B_r$  component (expressed by means of island width  $w$  dependence). It is also evident that character of evolution is fully given by sign

of quantity  $\Delta'$ . This parameter is calculated iteratively from both plasma edge and its center, namely ideal MHD stationary equilibrium equation is solved to obtain  $\psi$ .  $\Delta'$  represents discontinuity of both solutions at the edges of magnetic island where ideal MHD loses its validity. However, correct analysis of island growth would lead to slightly different character than that of eq. 2.38, namely:

$$\frac{dw}{dt} = 1.66 \frac{1}{\mu_0 \sigma} (\Delta'(w) - \alpha w). \quad (2.39)$$

Parameter  $\alpha$  from previous equation depends on local plasma parameters and as far as linear theory is applicable, it remains constant. As for  $\Delta'(w)$  its typical evolution (along with the other term as well) is shown in fig. 2.9. This and eq. 2.39 imply that in boundaries of linear theory, resistive MHD islands may grow only up to their saturated widths, upon which any further linear growth is inhibited. For island to overcome this saturation constraint and thus to grow to large amplitudes, interference from other phenomena (such as high  $j$  gradient near the island due to sawtooth relaxation) is necessary, so that linear theory used in derivation of this constraint is no longer valid.

As for characteristic growth time  $\tau_g$  of emerging islands, proper analysis would once again go beyond scope of this paper, and in the case of interest is to be found in refs. [4, 7, 8, 12] etc. Sufficient approximation of  $\tau_g$  of  $m = 2$  island on large aspect ratio tokamak can be in form (see [4]):

$$\tau_g \approx 4.5 w a T_e^{3/2} \quad \text{where } T_e \text{ is in keV} \quad (2.40)$$

Literature [8] (among many) identifies the tearing mode instabilities (or resistive tearing modes RTM) described above to be (also) cause of Mirnov oscillations. Their existence was first observed on large circular cross section tokamak T-3 by Mirnov and published in ref. [13] by Mirnov (and Semenov). On diagnostics outputs they exhibit typical behavior of magnetic islands located at plasma edge, such as periodical perturbations of poloidal magnetic field across the circumference, as can be seen in fig 2.10. Mirnov oscillations emerge during current ramp-up phase of the discharge and are in fact series of magnetic islands whose poloidal number  $m$  decreases with decreasing  $q_a$  at the plasma edge. For large aspect ratio tokamak of circular cross section, relation between  $I_p$  and  $q_a$  is trivial form of eq. 2.33, nonvariant on peaking parameter  $\nu$ :

$$q(a, t) = \frac{2\pi a^2 B_T}{R\mu_0 I_p(t)}.$$

given that plasma is centered in the chamber. Nevertheless it should be noted that magnetic islands emerging as Mirnov instabilities can (and do) persist even beyond the current ramp-up (see evidence in ref. [13]).

## Chapter 3

# Tokamak GOLEM Characterisation

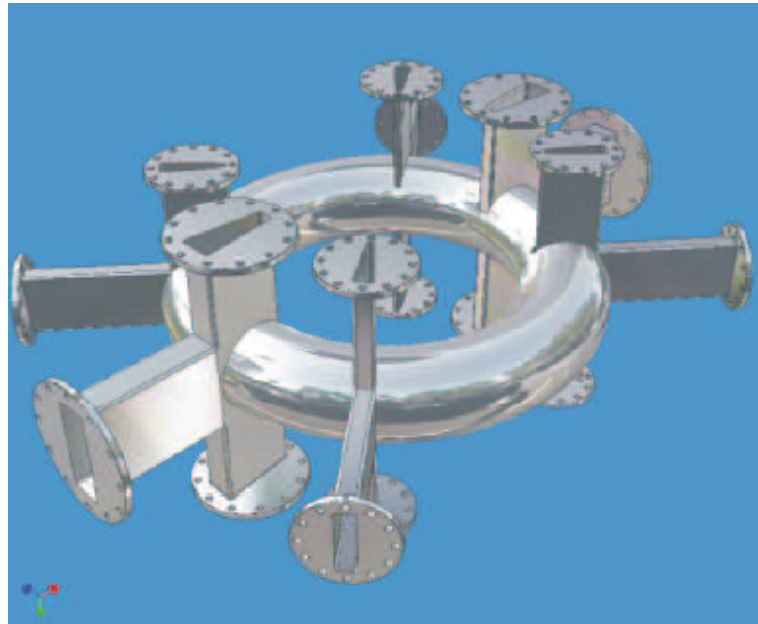


Figure 3.1: Model of GOLEM chamber with all the 16 ports depicted [15].

Tokamak GOLEM was one of the first constructed tokamaks and in fact currently is the longest operational tokamak. For reference purposes, until 2007 was this tokamak known as CASTOR (see ref. [14]) and used for edge plasma studies. However, its origin lies in Kurchatov Institute in Moscow, where it was used under the name of TM-1 MH to study plasma–microwave interaction. Its age implies that tokamak GOLEM is small tokamak of large aspect ratio and circular cross-section chamber (even though the chamber had to be replaced once before, it retained its geometry and dimensions). Exact parameters of its chamber (see ref. [15] e.g.) are  $R = 0.4$  m major radius and  $a_L = 0.1$  m of minor radius.

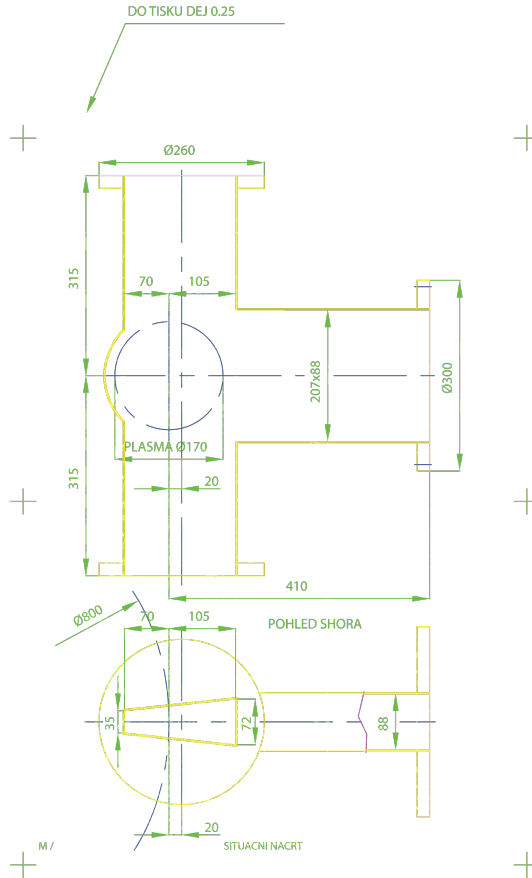


Figure 3.2: Blueprints of sets of large GOLEM diagnostic ports (in Czech).

Tokamak is of limiter configuration with two different circular limiters to choose from –  $a_1 = 0.085$  m and  $a_2 = 0.060$  m. Circular cross-section chamber with limiter configuration and of such a large aspect makes this tokamak closer to Alcator-A and T-3 mentioned in previous sections (and in refs. [6, 13]), than to modern tokamaks. Therefore, theory presented in previous sections should be more accurate towards analysis of tokamaks similar to GOLEM rather than to more recent tokamaks.

The chamber itself is made of stainless bellows steel, port holes taking more than 14 % of inner surface of liner (see ref. [16]). As can be seen from model in fig. 3.1, there are 16 diagnostic ports altogether, placed symmetrically on opposite sides of the chamber. Tokamak GOLEM has two different sizes of the port sets - two large sets and four smaller ones (for their exact dimensions, see blueprints in figs. 3.2, 3.3). Chamber enables to reach levels of vacuum corresponding to pressure  $\approx 3$  mPa and  $H_2$  work gas is injected to  $\approx 20$  mPa pressures. While work gas pressures correspond to recent tokamak experiments, vacuum level pressure still persists on one order higher magnitudes than it

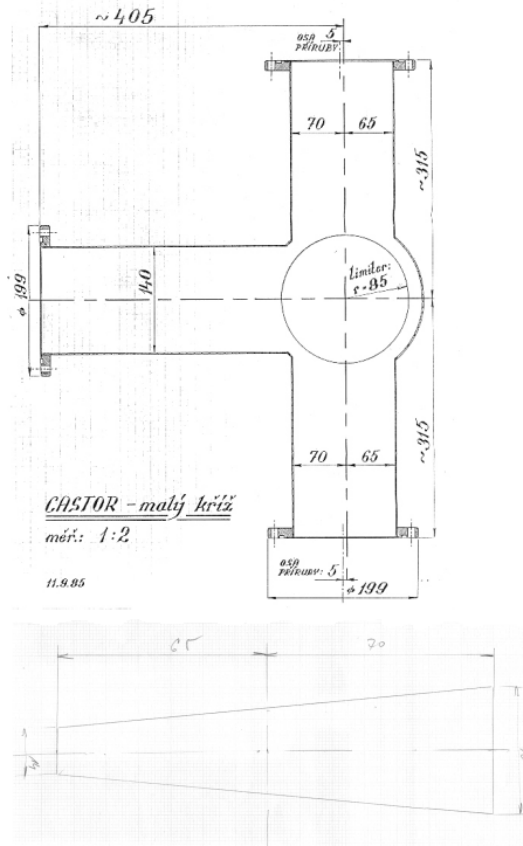


Figure 3.3: Blueprints of sets of small GOLEM diagnostic ports (in Czech). View from above is included in the lower part of the figure.

used to in IPP AS CR.

### 3.1 Discharge Properties and Magnetic Fields of Tokamak GOLEM

Basic parameters of discharge and plasma of standard GOLEM shot can be seen in fig. 3.4, representing  $U_{loop}$  loop voltage on low field side (LFS),  $I_p$  total plasma current,  $H_\alpha$  visible radiation of H gas and  $B_T$  central toroidal field magnitude. By comparison of these values to the ones stated in [17] of  $B_T = 1.1$  T,  $I_p = 10$  kA it can be seen that GOLEM currently operates on halved parameters than in IPP times. This is due to limited capacity of power supply systems that is currently available. Power systems are

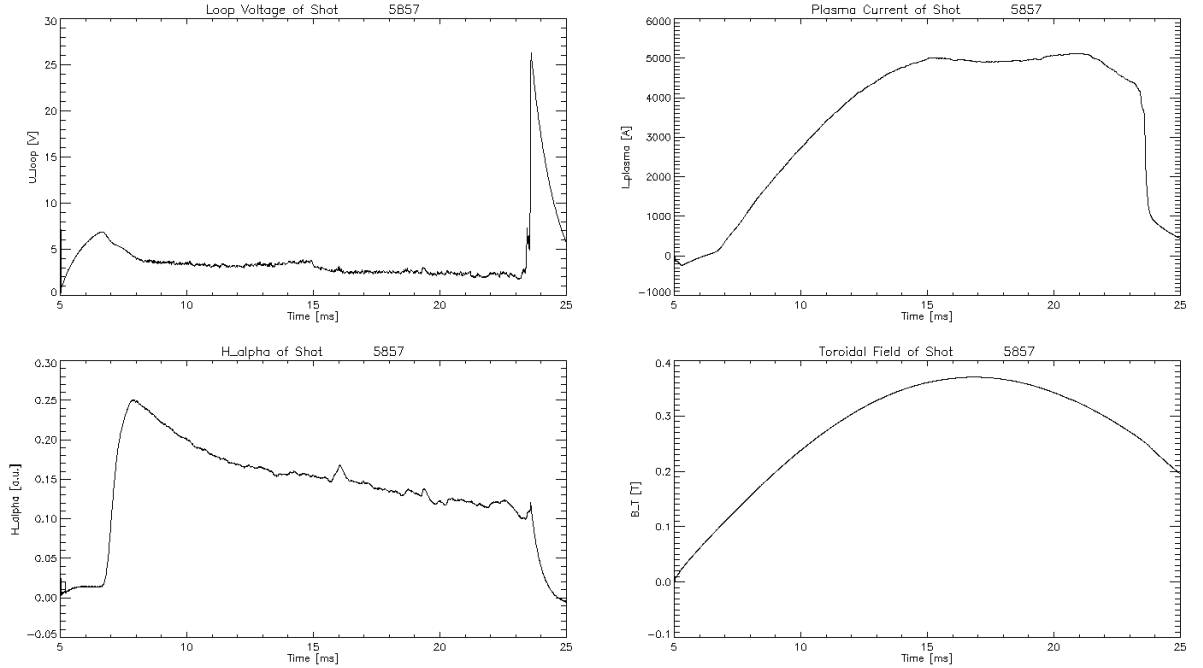


Figure 3.4: Typical evolutions of basic GOLEM discharge parameters (with passive stabilisation turned on in 15<sup>th</sup> ms).

represented by sets of parallel capacitors. Principial engineering scheme with respective total capacities (from the last year, since there has been an increase in  $B_T$  supply system capacity) is shown in fig. 3.5.

All of these systems power their respective set of magnetic field generation coils. Poloidal magnetic field coils are referred to as stabilisation coils and there are 3 different sets – see fig. 3.6. For  $I_p$  direction depicted in fig. 3.6, effect of generated magnetic fields by these windings is to push plasma towards HFS ( $B_V$  field) and bottom ( $B_H$  field).  $B_H$  field is generated by purple windings of 4 turns on each coil, while  $B_V$  field generates two sets of windings – black one with two turns on each coil placed outside the coating and the inner one with single turn on each coil, placed under the coating. There are known issues with too high magnitudes of poloidal field vector components (with respect to model) being detected on some locations on limiter radius. This occurs when field in question is generated by the coils placed outside of coating (for more detailed anaysis see ref. [18]). The problem was discovered during second half of last decade and the cause is yet to be understood. Several hypotheses to explain this have been proposed, but they still need to be experimentally investigated.

Here, it should be noted that by model of magnetic field it is referred to magnitudes

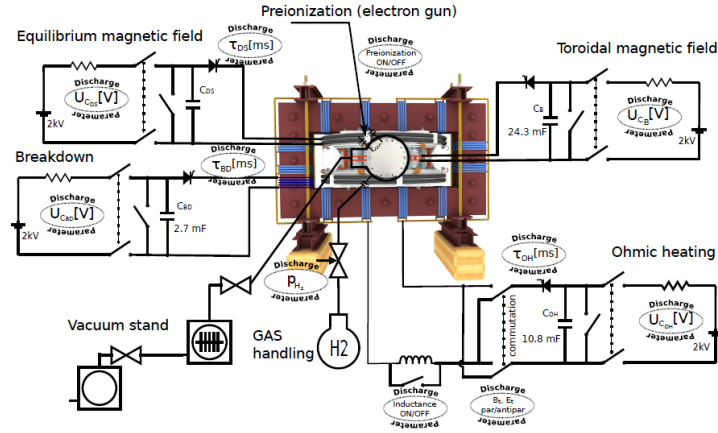


Figure 3.5: Engineering scheme of tokamak GOLEM with respective control parameters. Taken from ref. [14].

of respective component of  $\mathbf{B}$  vector given by application of Biot-Savart's law in form:

$$\mathbf{B} = \frac{\mu_0}{4\pi} I_{coil} \oint_l \frac{d\mathbf{l} \times \mathbf{R}}{|\mathbf{R}|^3} = A_{const} \cdot I_{coil},$$

on coil generating the field in question. Integral is calculated numerically by division of the coil into large number of infinitesimal elements of straight wire (usually at least  $\sim 10^4$  elements in less extensive models), calculation of contribution of this element represented by expression in integral while  $\mathbf{R}$  stands for 3D location vector between this element and point of reference and by subsequent summation of all the contributions. Advantage of this method is, that integral represents only spatial configuration and is independent on variable temporal quantities such as  $I_{coil}$  and thus for given reference point needs to be calculated only once –  $\mathbf{B}$  evolution then obtained by multiplication with coil current evolution.

This model, applied on  $B_V$  field generated by inner coils, seems to be in good agreement with measurement – see fig. 3.7. Series of measurements have shown that magnitude of measured  $B_V$  in the center of chamber is  $85.81 \pm 0.37$  % of expected magnitude. Obtained thumb rule between coil current and resultant field:  $B_V$  [T] =  $4.89 \cdot 10^{-6} \cdot I_{coil}$  [A]. By using observed  $\approx 86$  % agreement between model and series of measurements, this yields final relation of  $B_V$  [T] =  $4.20 \cdot 10^{-6} \cdot I_{coil}$  [A].

$B_T$  field is generated by set of 28 copper coils with 8 turns each, having inner radius of 16.7 cm. As for toroidal magnetic field profile,  $1/R$  decrement relation is widely used in practice. This dependence can be obtained by application of Ampere's law on

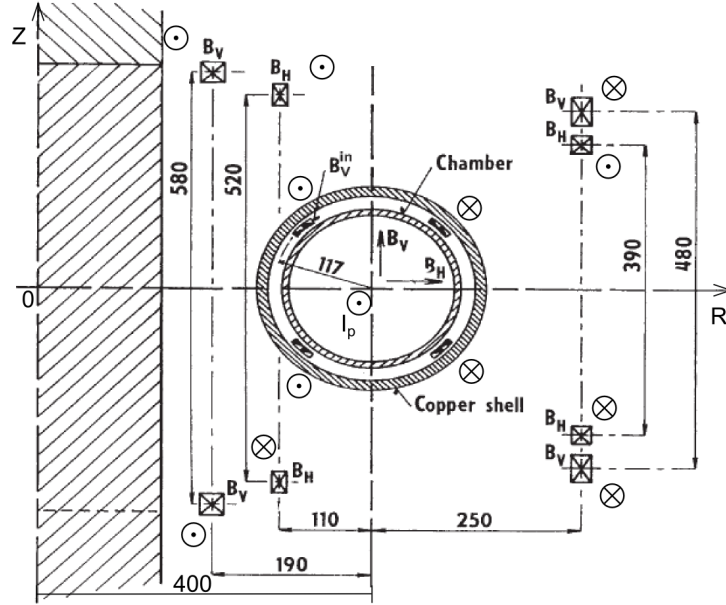


Figure 3.6: Blueprints of poloidal cut through tokamak, with locations of stabilisation poloidal field coils and respective current and generated field directions.

total current in coils of toroidal field placed around major axis assumed to represent an infinitely long thin wire. This assumption might be excusable for central midplane (i.e. at  $Z = 0$  coordinates) on D-shaped tokamaks, however in the case of large aspect ratio tokamak of circular cross-section this may no longer be the case, especially on the top or bottom of the chamber. Therefore, a relatively complex model based on Biot-Savart's law was developed to provide full poloidal profile (not only bound to  $Z = 0$  plane) of  $B_T$  magnitude. In the model, the poloidal profile is represented by  $60 \times 60$  grid with physical dimensions covering space beyond the outer radii of the coils. Grid is placed on fixed toroidal angle, however in calculation of contribution of all the 28 coils their different toroidal locations must be taken into consideration. Each of the coils is divided into 8 turns of different radial coordinates (corresponding to real dimensions of the coils) with every turn divided into  $10^3$  elements, meaning that for each of 3600 grid points, contribution from  $224 \cdot 10^3$  elements of different location and orientation in 3D space had to be summed. There were modelled two planes altogether at different toroidal angles, corresponding to location between coils – diagnostic port location or location of the lowest expected magnitude at the edge and location right under one of the coils – location of toroidal flux sensor or location of the highest expected magnitude (see fig.

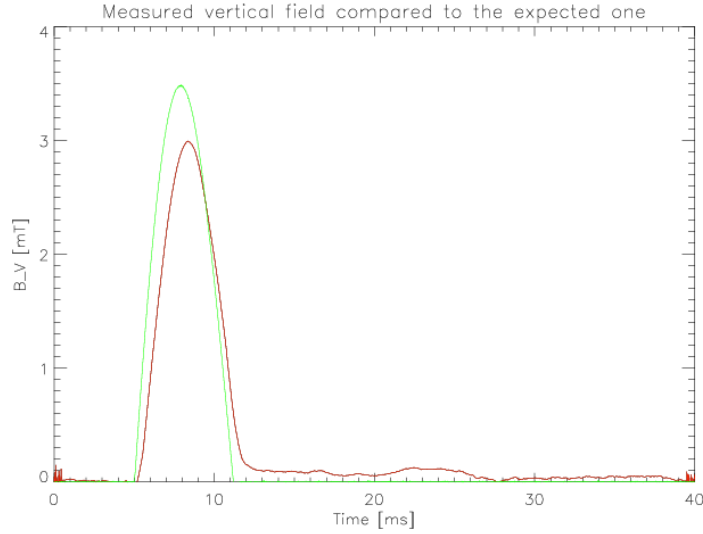


Figure 3.7: Comparison of measured magnitude of  $B_V$  generated by inner stabilisation coils (red line) to values given by application of Biot-Savart's law on their spatial configuration and currents (green line).

3.8). Character of poloidal profile seems to have toroidal ripple and the top and bottom of the plot is far from  $1/R$  dependence, however total toroidal magnetic flux  $\chi$  flowing through coil radius is in both modelled poloidal planes practically the same - only 4.2 % difference was found, despite using two most different planes. Not to mention that difference towards  $1/R$  profile is in both cases less than 2.3 %. Main cause of this is that over most of the poloidal plane,  $B_T$  profile retains  $1/R$  dependence, as can be seen in fig. 3.9 (for  $Z=0$  locations). Since coil radius is 16.7 cm and maximal possible limiter radius is  $a_1 = 8.5$  cm, model implies that GOLEM is by construction a zero-ripple tokamak. As for experimental evidence, an actual measurement of  $B_T$  profile on  $Z = 0$  plane at diagnostic port toroidal angle (between two  $B_T$  coils) was carried out as well, with results in fig. 3.9. From the measurement it seems that actual magnitude of  $B_T$  field is a little lower across all the measured  $R$  locations (1-5 % across the limiter). It also implies that there might be some degree (however small) of toroidal ripple even on limiter location.

Likewise in the case of  $B_V$  field, there exists a thumb rule for central  $B_T$  calculation as well, since Ampere's law is of same character as Biot-Savart's law –  $B_T$  [T] =  $1.12 \cdot 10^{-4} \cdot I_{coil}$  [A], where  $I_{coil}$  represents current from capacitors (single wire) and not the total current in all the turns of each coil. Once again, this thumb rule can be normalised to represent measured values, in which case it yields  $B_T$  [T] =  $1.09 \cdot 10^{-4} \cdot I_{coil}$  [A]. For

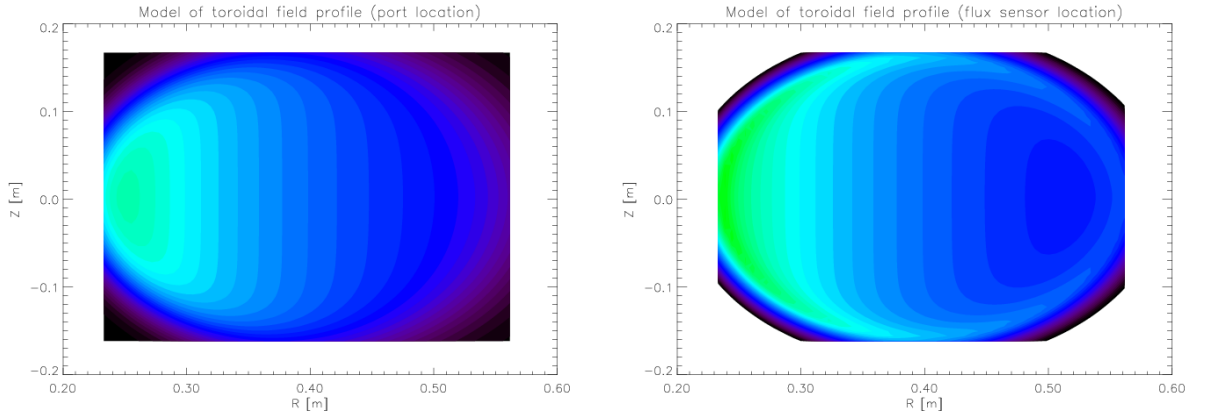


Figure 3.8: Model of  $B_T$  profile across the whole poloidal cross-section. Left plot corresponds to toroidal location of modelled poloidal plane under one of diagnostic ports (between two  $B_T$  field coils), while plot on the right represents toroidal location under  $\chi$  toroidal flux sensor (under one of  $B_T$  coils).

poloidal magnetic field at plasma edge, it is straightforward to obtain that  $B_\theta(a_1)$  [T] =  $2.35 \cdot 10^{-6} \cdot I_p$  [A] and  $B_\theta(a_2)$  [T] =  $3.33 \cdot 10^{-6} \cdot I_p$  [A] (depending on limiter used). Thus plasma currents on GOLEM, this typically yield  $B_\theta \approx 10$  mT. As for perturbative radial field, it is yet to be investigated on GOLEM, nevertheless for estimative purposes, magnitudes measured on CASTOR can be used. Ref. [19] states that this value is  $\approx 1$  mT. Together all of this yields the most illustrative thumb rule for tokamak GOLEM, i.e.  $B_T \sim (5 \cdot) 10^2$  mT,  $B_\theta \sim 10^1$  mT and  $B_r \sim 10^0$  mT.

## 3.2 State and Calibration of Magnetic Diagnostics of Tokamak GOLEM

For studies of MHD instabilities, magnetic diagnostics play critical role, not to mention that the most basic global discharge parameters are currently determined by means of magnetic field detection. Namely  $I_p$  which is measured by Rogowski coil encircling the coating (i.e. measures sum of liner and plasma current),  $U_{loop}$  measured by flux loop placed on LFS and central  $B_T$  standardly measured by small coil reacting on vacuum field on LFS (however after a successful calibration of magnetic diagnostics as a whole, there is now a wide variety of means of  $B_T$  measurement). All the standardly operated

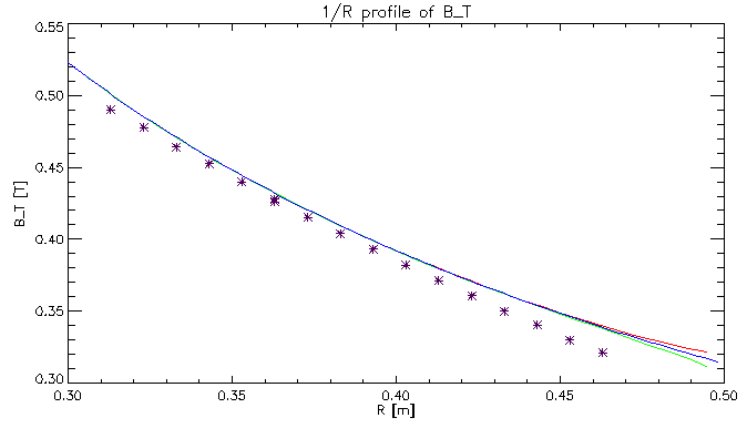


Figure 3.9:  $B_T$  field  $1/R$  profile at  $Z = 0$  (i.e. central midplane) with  $R$  limited by liner dimensions. All the magnitudes correspond to 3500 A peak of  $B_T$  capacitors discharge current output and thus represent typical magnitudes of GOLEM discharge. Blue line represents  $1/R$  of Ampere's law, green line profile on the left in fig. 3.8, red line profile on the right in fig. 3.8 and purple asterix directly measured values by 3D Hall probe.

magnetic diagnostics sensors of tokamak GOLEM (not including industrial class current sensors) are of inductive nature, meaning they measure temporal rate of change of  $\mathbf{B}$ , being based either on Ampere's law (Rogowski coils) or on Faraday's law (flux loops and local  $\mathbf{B}$  sensors). To obtain the respective sought quantity (except for loop voltage), their signal has to be integrated – i.e. the measured voltage must be integrated over both the total effective surface of the loops and the temporal evolution. This is currently carried out solely by numerical means, which in the case of temporal integration part may be effective only under condition that data acquisition sampling rate is fast enough to cover all the changes in signal. This seems to be the case in all the basic diagnostics, as 100 kHz rate is standardly applied. Unfortunately, plasma fluctuations seem to require rate at least an order higher, resulting into measurements of local  $B_\theta$  to be very challenging to process and successfully interpret.

This difficulty might be partially caused also by low signal/noise ratio on Mirnov coils (MC) – detectors of local  $B_\theta$  and MHD activity. It is peculiar that prior to experience and investigation, noise magnitudes seem to be caused by some source outside the tokamak systems and fluctuate with characteristic time  $\sim$  days. Some experiments concerning replacement of coaxial cable connecting sensor and data acquisition system

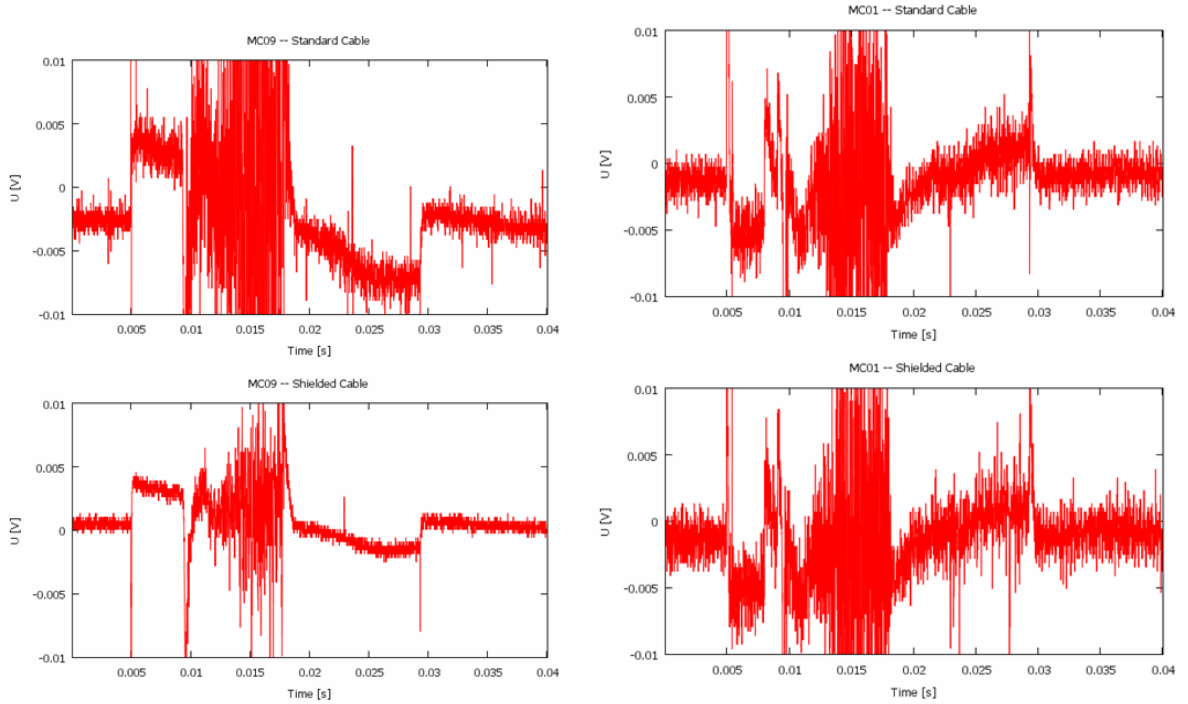


Figure 3.10: Two essentially same signals of  $B_T$  cross-talk and plasma signal on Mirnov coil 9 (HFS location) and Mirnov coil 1 (LFS location) acquired by different cables.

(DAS) with provisory shielded cable were carried out on two of the detector coils (results are summarised in fig. 3.10). For the whole set of control discharges and cable replacing procedures, character of influence of shielding on noise magnitudes seem to depend on coils themselves. While on MC09 coil, a significant noise reduction was observed every time the shielded cable had been applied, MC01 coil did not show any reaction whatsoever. Notation and locations of Mirnov coils can be seen in fig. 3.11.

Basic principles of magnetic diagnostics according to refs. [20, 21], as well as basic properties of sensors in question (such as available sensors, their geometrical dimensions and transformation relations of their signal into measured quantities) have already been described in ref. [18]. Nevertheless, there have been some changes, calibration and observations since last year, which should be described. First of all, it was observed that  $B_T$  signal cross talk on Mirnov coils due to their misalignment (namely  $K_C$  constants representing ratio of cross talk signal magnitude to magnitude of  $B_T$  detection coil signal) have changed significantly and thus need to be regularly updated with sets of calibration shots (i.e. discharges without plasma and with only  $B_T$  field present). Additionally, a voltage divider was placed on flux loop, meaning that measured signal of  $U_{loop}$  needs to

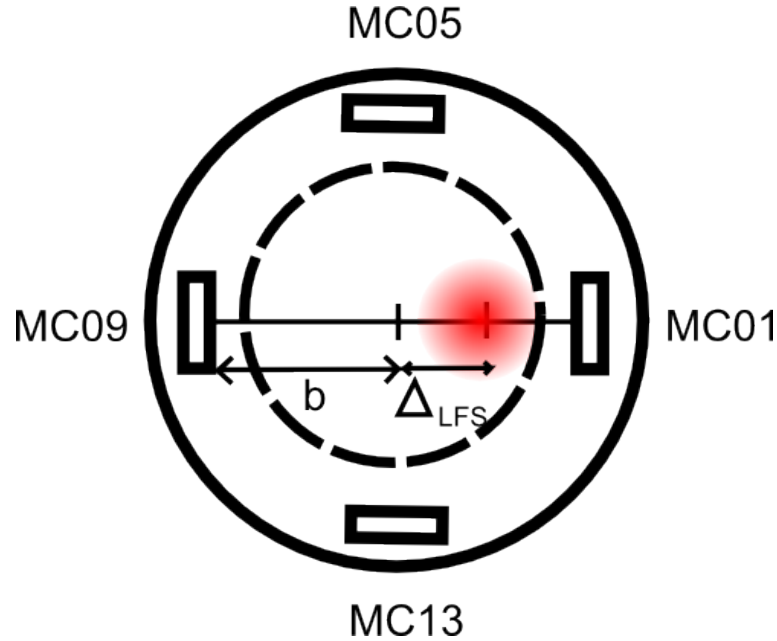


Figure 3.11: Spatial distribution and notation of available Mirnov coils (MCs) across the whole poloidal circumference.

be multiplied by factor of 3.75 to correspond to real values of measured quantity. It was also discovered that there is another voltage divider (hardly visible) on sensor of total toroidal flux  $\chi$  thus signal of this sensor must be multiplied by factor of 2.00. This sensor was then used to validate, whether Biot-Savart's model approach to  $\chi$  poloidal profile corresponds better to measured values than  $1/R$  approach by Ampere's law. As can be seen in fig. 3.12, the more complex model indeed describes reality slightly better than the simpler one. The most important change is that small coil of central  $B_T$  measurement was absolutely calibrated by direct measurement of this quantity (this was actually the main purpose of the whole calibration session) to  $(70.42 \pm 0.90)$  T/Vs (i.e. T on integrated raw signal). This transformation coefficient proved to be invariant on magnitude of applied  $B_T$ . Obtained relation is more straightforward to use than relation based on  $I_{coil}$  introduced in previous section (though the result is the same).

During experimental session with limiter of smaller radius ( $a_2 = 0.06$  m), there were 4 channels of fast data sampling rate of 1 MHz (represented by an oscilloscope) available, which were used for MC data acquisition. Unfortunately their use introduced inexplicably variable offsets into measured data which caused that temporal integration of measured MC signals was not possible. Fortunately, for purposes of MHD activity analysis (primarily represented by Fourier transform and cross-correlations) rate of change of local

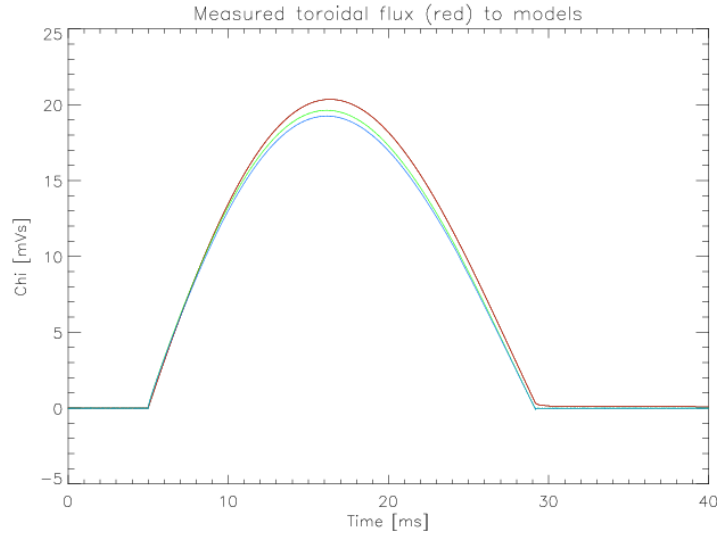


Figure 3.12: Comparison of measured total toroidal flux  $\chi$  (red line) to model by Biot-Savart (green line) and by Ampere (blue line).

$B_\theta$  was more than sufficient.

Nevertheless, a new data acquisition system, characterised by higher sampling rate and channel count than the currently used one will be implemented in near future. Additionally a new set of local  $\mathbf{B}$  sensors is under development. This includes 16 new Mirnov coils (with possibly analogue integration of measured signal, would it prove to be necessary despite higher sampling rate of new data acquisition system) for local  $B_\theta$  measurements for plasma position and MHD analysis purposes and 4 sets of 3D (i.e. 3 orthogonal probes in each set yielding 12 probes altogether) high temperature experimental Hall probes for ITER R and D purposes (possibly trilateral collaboration between FN-SPE, Poznan Technical University and IPP AS CR). Exact parameters of semiconducting material in question will be known upon their arrival in the near future, nevertheless they will be characterised by wide temperature range of operation: -270 to 300 C compared to current -40 to 100 C, while retaining magnetic field sensitivity of high quality sensors – both in absolute values and in change with temperature. Their susceptibility to radiation damage will of course need to be investigated as well (preferably in a fission reactor). Sensitive semiconducting material will be shielded from GOLEM plasma by being encased in  $\text{Al}_2\text{O}_3$  (corundum) cubes. Both the new MC array and extended temperature Hall sensors (ETHS) are to be fixed on an improved support construction, shown in fig. 3.13. Construction is supposed to be robust enough to withstand strong Lorentz force shocks of GOLEM discharges (in contrary to the previous one). It is made of industrial

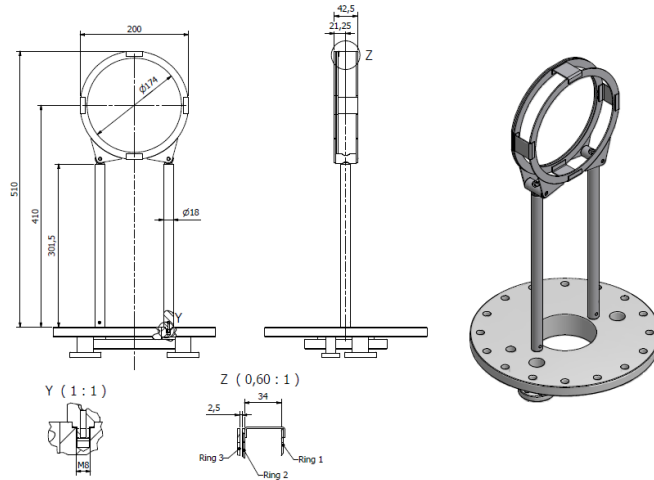


Figure 3.13: Final blueprints of new support construction for new set of 16 Mirnov coils and 4 3D Hall probes (made by *Vakuum Praha*).

stainless 316L steel of non-ferromagnetic properties (processed by means of laser cutting to prevent event. ferromagnetisation), standard material used in tokamak research and the same material used for ITER chamber walls (as a main support construction, not the first wall component, though). The previous construction of diagnostic ring enabled to hold array of large number of Langmuir probes and this could also be the case of the new construction as well. Nevertheless, priorities of construction were in sequence: stability, ETHS, MC, Langmuir probes, and thus space for Langmuir probes was reduced in favor of magnetic probes.

# Chapter 4

## MHD Activity of Different Shot Regimes

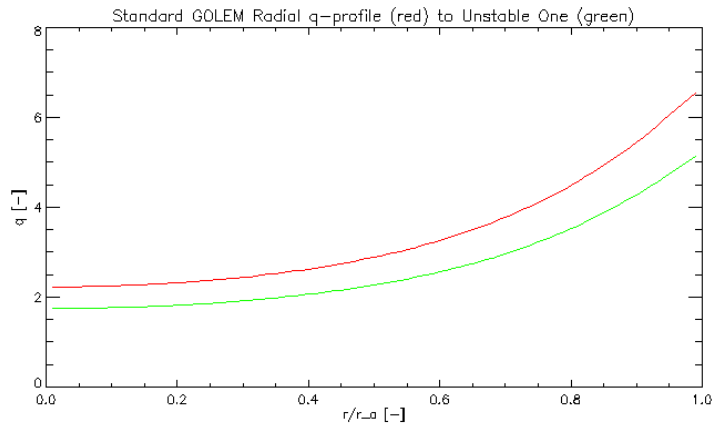


Figure 4.1: Radial  $q$ -profiles for standard GOLEM operational parameters of  $B_T = 0.37$  T,  $I_p = 5$  kA,  $a_1 = 0.085$  m (red), and for parameters of small limiter discharge  $B_T = 0.35$  T,  $I_p = 3$  kA,  $a_2 = 0.060$  m (green) given that  $\nu = 2$  in both cases.

As was mentioned in section 2.1, MHD instabilities tend to cause change of magnetic surfaces topology, so that magnetic islands emerge on rational  $q_s = m/n$  surfaces. When rational  $q$  is radially located near plasma edge, it is possible to detect respective magnetic island by means of local  $B_\theta$  sensors as periodical perturbations of signal across the plasma circumference. This periodicity is due to rotation of island, caused both by plasma rotation and by inherent rotation of the island (with respect to plasma) – see ref. [4]. Standard sensors of perturbed  $B_\theta$  measurement are represented by set of at least 14

magnetic signal pick-up coils, often referred to as Mirnov coils as for such purposes they were used for the first time in publication [13]. Since there are currently only 4 operational MC on tokamak GOLEM, it is not possible to determine poloidal mode no.  $m$  of detected islands (neither toroidal mode no.  $n$  as all the coils are localised on single toroidal location) in the same manner as it was carried out in fig. 2.10. Nevertheless, it is possible to estimate expected island mode number by use of relation 2.33, its spatial dimensions with eq. 2.9 and resultantly its characteristic growth time into saturation width by relation eq. 2.40. Two different regimes of GOLEM operation are analysed, each corresponding to one of the two different available limiters. Peaking factor of GOLEM current density (and pressure) is assumed to be  $\nu = 2$ , which for respective discharge parameters of given limiters yields radial profiles in fig. 4.1. Such high  $q_a$  values are not ideal for MHD instability studies, since  $m = 3$  and  $m = 2$  islands are of main interest (and of main influence on plasma stability). This is due to  $I_p$  magnitudes for small limiter being 33 % of values in ref. [19], where these islands have been investigated, while  $B_T$  being only halved. Unfortunately, it proved that lowering of  $B_T$  in order to reach lower  $q_{edge}$  was contraproductive, since plasma confinement degradation was too severe for islands to develop. Since  $m$  numbers are of so high value, only islands present at the plasma edge will be investigated, as  $m = 2$  islands are below sequence of several rational  $q$  surfaces. Thus island widths respective to limiter radii (by taking estimation of  $\widehat{B}_r \approx 1$  mT) of  $m = 6$  and  $m = 5$  numbers according to eq. 2.9 are 33.62 % for  $a_1$  and 39.99 % for  $a_2$  respectively. Since ref. [4] uses as an example the largest island width of  $m = 2$  island to be typically of 10 % of limiter radius, it seems that approximation used relation is not fit for estimation of GOLEM island widths. If this relation is applied on CASTOR discharge parameters stated in ref. [19] (using  $a_2$  limiter) corresponding to  $m = 3$  island at the plasma edge, island of size of 29.20 % of  $a_2$  is obtained. It is interesting that by multiplication of  $B_T$  by factor of 2 and  $I_p$  by factor of 3, the estimated width of island has shrunk by one third. Not to mention that results of calculation applied on real-life large aspect ratio tokamak data contradict to statement in ref. [4] that island width drops with increasing  $m$ . This could imply that estimation of island dimensions by relation 2.9 would be valid only for small  $m$  number islands. Estimation of growth time  $\tau_g$  from relation 2.40 can not be applied on currently achievable GOLEM discharges as it corresponds only for growth time of  $m = 2$  islands and global parameters suggest that such islands are not present anywhere near limiter radii. The relation can not be straightforwardly modified for other  $m$  values as  $r_s \Delta'$  parameter, necessary for  $\tau_g$  estimation has to be calculated numerically and available literature (refs. [3, 4]) states values calculated only for  $m = 2$

islands since these are of main interest. Nevertheless, by application of this relation on old CASTOR discharge parameters, it yields  $\tau_g \approx 1$  ms in comparison to 40 ms discharge time.

In order to obtain insight into overall MHD activity of tokamak GOLEM, it was necessary to carry out complex analysis of largest variety of shots possible. For such purposes, a database of total 46 different GOLEM discharges was assembled and thoroughly analysed. Chosen discharges were divided into 7 categories of: calm shots without passive stabilisation, shots with fast DAS and small limiter, shots of high  $U_{loop}$  magnitudes, shots of high initial H<sub>2</sub> pressure, shots with large  $U_{loop}$  fluctuations, shots with reversed passive stabilisation and finally shots with correctly applied passive stabilisation. Shots were analyzed both by standard means of global parameters and by slightly more advanced statistical methods of Fourier transformation and correlation analysis. From perspective of the latter methods, new relevant information on plasma behaviour had been contained only in calm discharges without stabilisation, discharges with passive stabilisation (of plausible orientation) and in small limiter-fast DAS studies. As for other categories, upon analysis they degenerated into one of the above-mentioned. In following subsections, characterisation of whole categories will be demonstrated on an example of analysis of typical shot.

## 4.1 Calm GOLEM Discharge Without Stabilisation

Calm discharges without passive stabilisation used to be set as an example of typical GOLEM discharge. Relevant parameters of discharge analysis (with exception of visible radiation) are presented in fig. 4.2. From such parameters, resultant  $q$  profile would correspond to the standard one of the two in fig. 4.1. It is evident that this shot was terminated by sudden major disruption event (followed by according sound effects as plasma hit  $a_1$  limiter. From comparison of local  $\dot{B}_\theta$  perturbations to  $I_p$  plasma current in fig. 4.2, gradual increase in their magnitude is (especially) evident during initial  $I_p$  rise period. This phenomenon is most likely due to growth of Mirnov instabilities described in section 2.3.2 as well as to growth of plasma column itself. By comparison of all the MC outputs during the initial current rise, there indeed seems to be spatial shift of signal across the poloidal circumference (corresponding to island rotations), biased with gradual frequency change (as islands of lower  $m$  emerge). Unfortunately, due to insufficient DAS

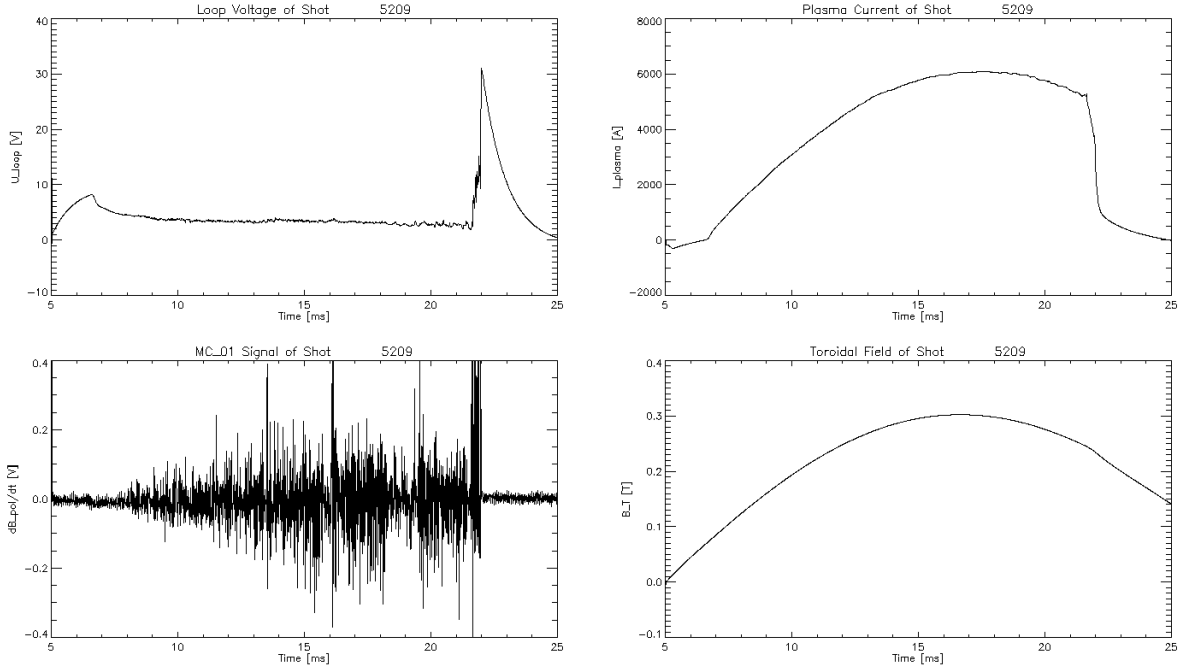


Figure 4.2: Plot of typical relevant parameters of stable shot without passive stabilisation enabled.

sampling rate, this phenomena could not be thoroughly analysed by cross correlations and thus the only relevant experimental evidence for this lies in section 4.3, where faster DAS could be applied. Additionally, by comparison of poloidal field fluctuations in fig. 4.2 to the ones in fig. 2.6 in section on disruptions, presence of magnetic islands at the plasma edge during current flat-top is suggested as well. Once again, higher sampling rate than available would be necessary for further investigation.

Nevertheless some insight can be obtained by carrying out the Fourier analysis of measured signals to obtain their temporal frequency distributions. All the MCs yield thus frequency spectrograms in fig. 4.3. These plots suggest that MHD activity signal detected on all the MC coils is initially of the same order across the whole poloidal circumference. However, amplitude of perturbations on LFS and top gradually increases, while on the HFS and bottom the fluctuations in signal seem to retain their magnitude up to the disruption event. The strongest perturbations correspond to frequencies above 20 kHz, however they seem to be single event fluctuations rather than oscillations caused by island rotation. Since fluctuations have limited dimensions, expected to be approximately of same magnitude across the poloidal circumference (see fig. 2.10), growth of their signal can be physically interpreted as shift of plasma column position towards detecting probe.

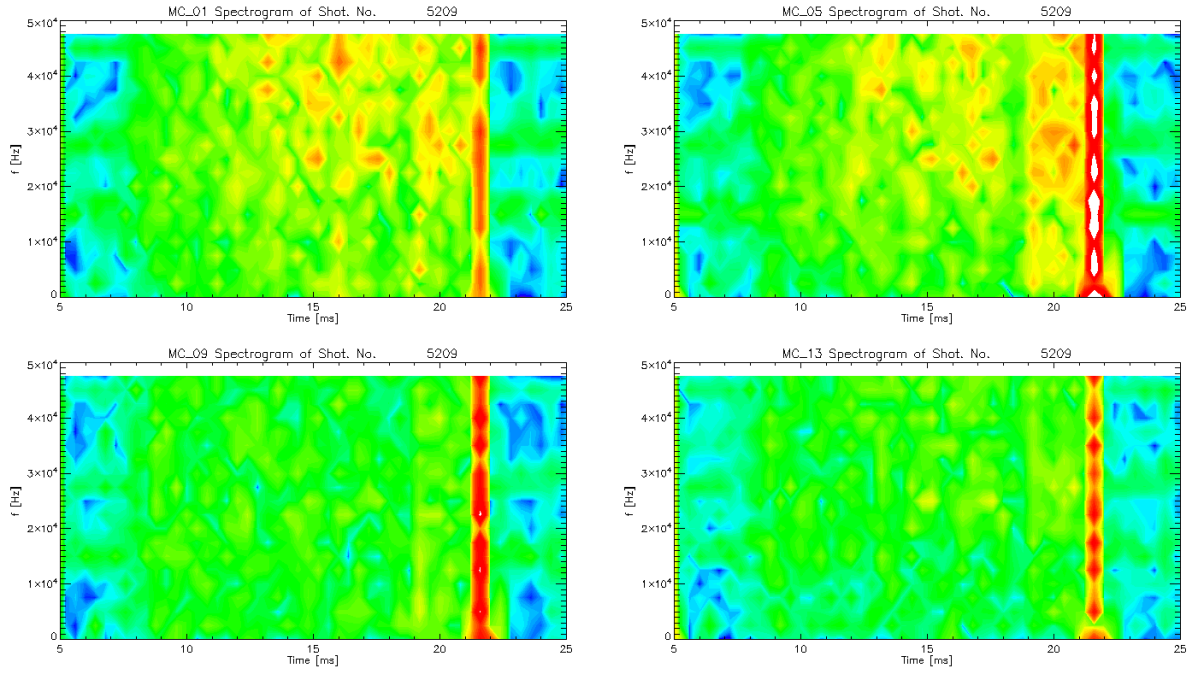


Figure 4.3: Frequency spectra of  $\dot{B}_\theta$  signal fluctuations detected by respective MCs.

Thus, according to Fourier analysis of frequency spectra, plasma seems to be gradually shifted towards LFS and top of the chamber.

## 4.2 GOLEM Discharge With Stabilisation

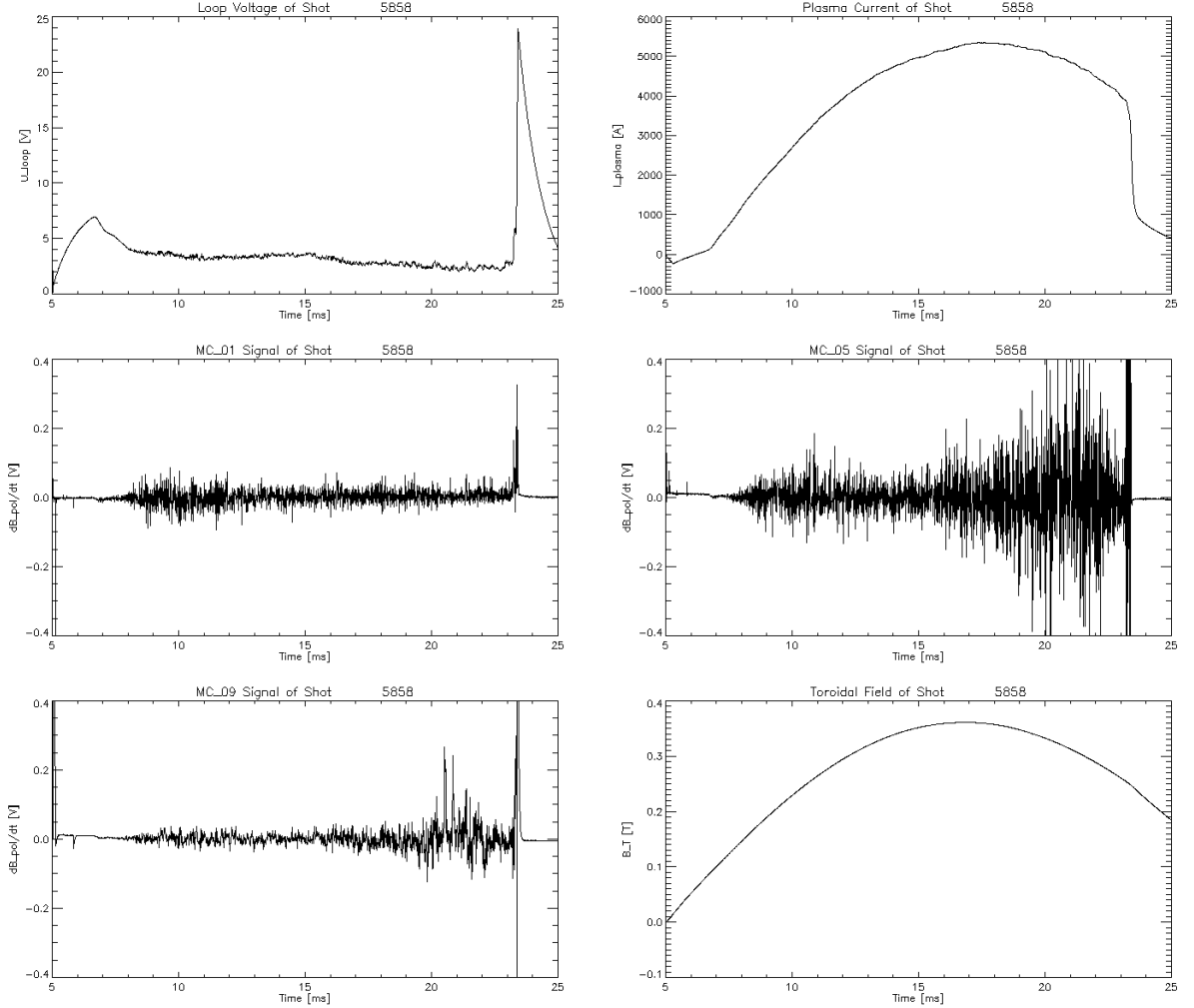


Figure 4.4: Plot of typical relevant parameters of stable shot with passive stabilisation turned on at 15<sup>th</sup> ms.

During analysis of discharges with enabled stabilisation, the time of stabilisation onset must be kept in mind. In the case of shot no. 5858, this corresponds to 15<sup>th</sup> ms. Measured evolution of stabilisation field in fig. 3.7 suggests that magnitude of stabilisation field reaches its maximum 3.5 ms upon initialisation, only to completely vanish after 6-7 ms upon its onset. Basic shot parameters of analysed discharge in fig. 4.4 seem to be approximately equal to the ones shown in previous section. However, there is clear drop in  $U_{loop}$  (i.e. improvement in plasma confinement) in the moment the stabilisation windings are energised. This trait is more evident on some shots than on others (provided all have similar plasma and stabilisation parameters) and the cause of this is yet to be

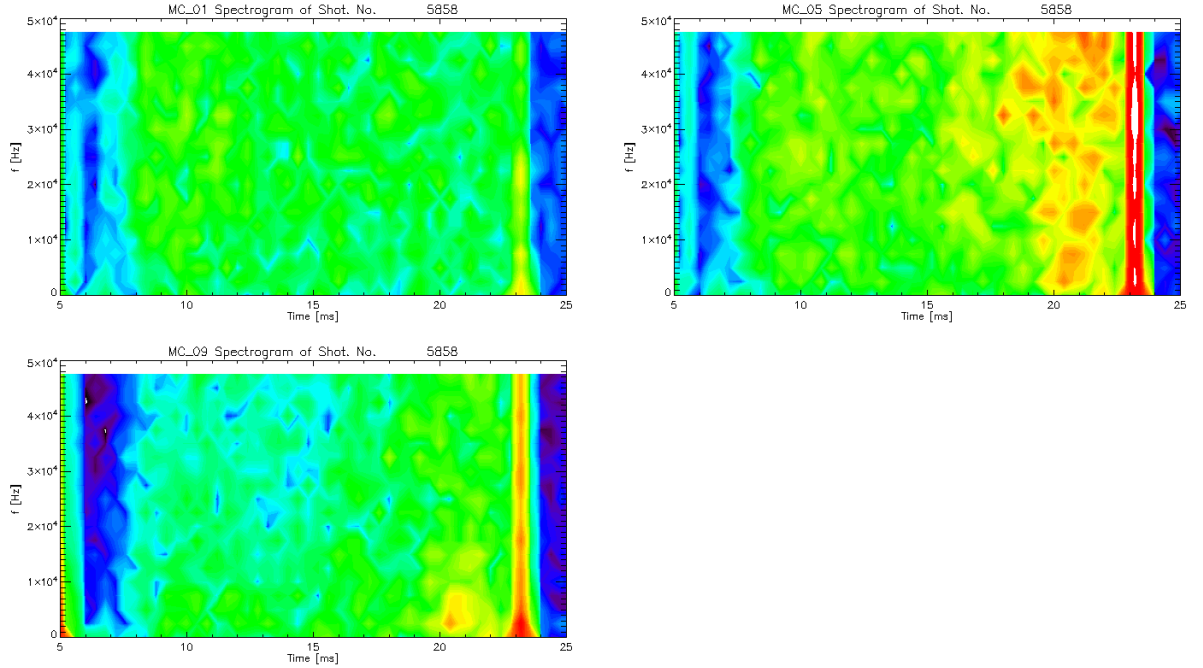


Figure 4.5: Frequency spectra of  $\dot{B}_\theta$  signal fluctuations detected by respective MCs.

understood.

Comparison of local  $B_\theta$  fluctuations in fig. 4.4 (that took place before onset of  $B_V$ ) to the ones in fig. 4.2 implies that during this session was plasma more stable in general. Additionally, variable signal/noise ratio between different sessions mentioned in section 3.2 is to be observed as well. As for correlation of MC signal fluctuations in fig. 4.4 to presence of  $B_V$ , instant response seems to be present only for MC05 located at the top (in form of fluctuations growth at it). However, analysis of signal frequencies in fig. 4.5 reveals crucial change in frequency spectra character evolution (with respect to discharges without stabilising  $B_V$ ). Frequency spectra character on plasma onset seem to be the same, however upon initialisation of  $B_V$ , fluctuations on LFS start to mitigate to negligible magnitudes while magnitudes on HFS seem to grow. This suggests shift of plasma column towards HFS due to Lorentz force arising from interaction of plasma current and  $B_V$  field. Even upon analysis of the whole database of 48 different discharges, this phenomenon seems to be connected exclusively to presence of plausible stabilisation field of vertical orientation, meaning that another evidence of positive influence of passive stabilisation field on GOLEM plasma confinement is obtained. Another important observation is that gradual shift of plasma column towards top seems to be unaffected.

Nevertheless, in the light of observed plasma reaction to  $B_V$ , it would seem that application of an additional horizontal magnetic field  $B_H$  in direction towards LFS (generated by coils located outside of coating) would lead to further improvement in confinement. It is strongly recommended to verify this hypothesis in the (possibly near) future.

Another physical phenomenon can be observed by comparison of MC09 signal frequencies in fig. 4.5 to the ones of MC01 of previous section in fig. 4.3. Fluctuations that grow on HFS are of an order lower frequency than those growing on LFS. This might be due to plausible magnetic field lines curvature on HFS (i.e. centrifugal force vector being parallel to pressure gradient) and to destabilising curvature on LFS (i.e. centrifugal force vector being antiparallel to pressure gradient) leading to variety of pressure instabilities (i.e. not of MHD character).

### 4.3 Unstable GOLEM Discharge with Small Limiter

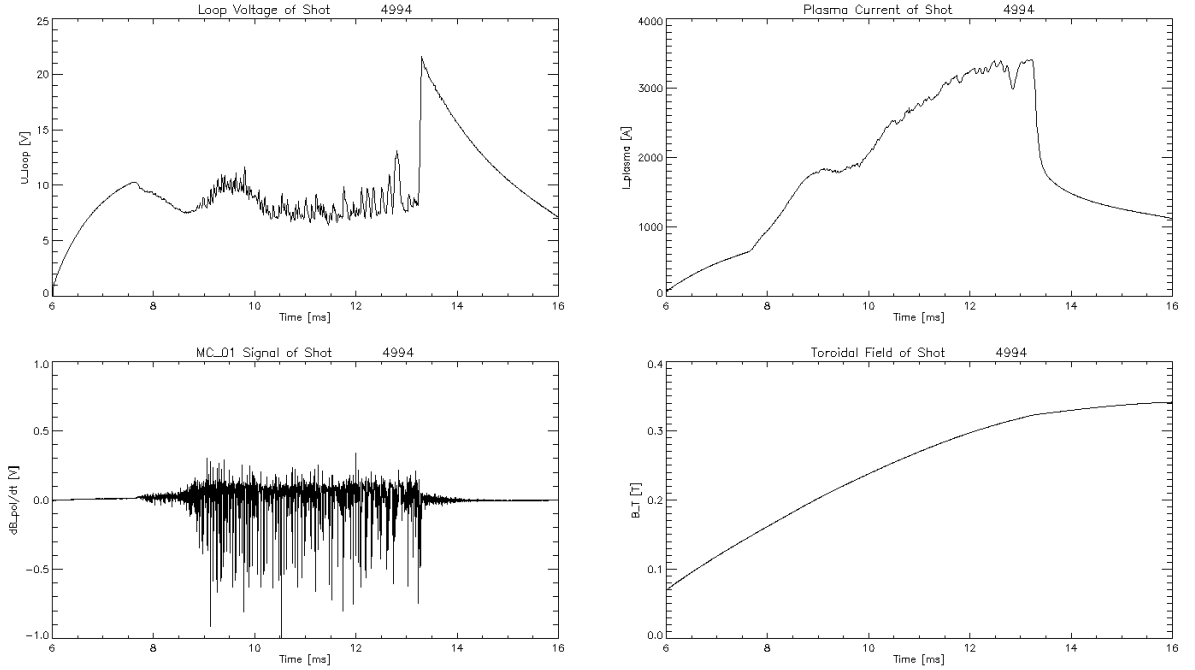


Figure 4.6: Plot of typical relevant parameters of small limiter GOLEM discharges.

During experimental session with small limiter, high data acquisition sampling rate of 1 MHz was available for MCs, enabling more detailed analysis of emerging instabilities. Basic parameters of discharge were different from the standard ones of tokamak GOLEM, as can also be seen in fig. 4.6, yielding  $q$  profile of the less stable shot as presented in fig. 4.1. The whole session was affected by increased impurities concentration inside of the chamber since small limiter (which is not used regularly) could not be thoroughly sanitized before introduction into liner and was used for the first time after several years. Additionally, due to the currently limited overall plasma confinement of tokamak GOLEM, plasma column often came into contact with Langmuir probes placed around this limiter, which resulted into sequence of minor disruptions (as can also be observed on  $U_{loop}$  fluctuations in fig 4.6). It should be noted that during the whole session, passive stabilisation field  $B_V$  was not applied and thus this session is the session of section 4.1 than to previous one.

Improved sampling rate critically improved relevance of statistical analysis outputs. Frequency range detectable by Fourier transformation of the signal has been widened (due to increase in Nyquist frequency) up to 500 kHz – see fig. 4.7. It can be seen that in

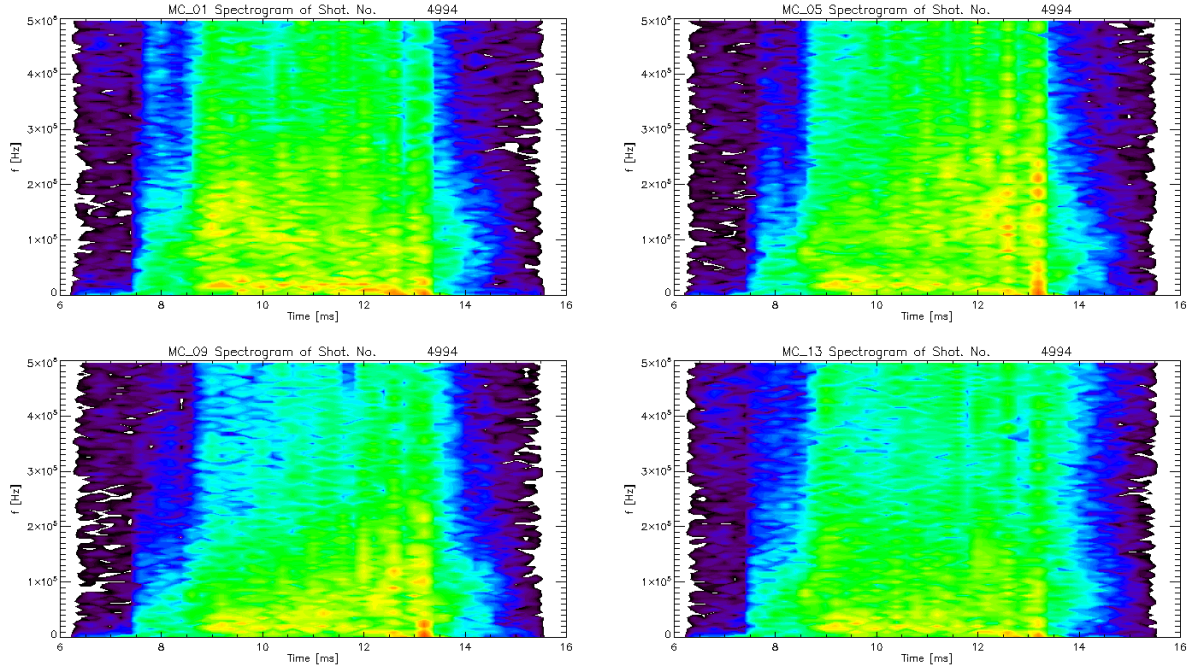


Figure 4.7: High sampling rate frequency spectra of  $\dot{B}_\theta$  fluctuations signal detected by respective MCs.

the absence of  $B_V$  stabilisation field, MC01 and MC05 signal fluctuations dominate even during this session, implying that plasma column retained its tendency to drift towards LFS and top. As was already mentioned, due to plasma interaction with limiter probes over most of the discharge, it is unlikely for most of the detected instabilities to be able to develop into magnetic islands. However during initial current rise, before the first minor disruption event, a variety of growing MHD instabilities can be observed. This can be detected over all of the frequency spectra as occurrence of perturbations of frequencies below 150 kHz, taking place between 7.5<sup>th</sup> and 8.5<sup>th</sup> ms – see fig. 4.7.

Despite all the merits of Fourier transform analysis of these instabilities, cross-correlation analysis yields better insight into their nature. By comparison of MC signals over the whole circumference in two different temporal sections of initial current rise, upper plots of fig. 4.8 are obtained. Widening of observed areas would show that gradually growing (due to plasma column growth) periodical oscillations with variable frequency (due to  $m$  change) are present during the current rise period as a whole, up to first minor disruption event. By calculation of cross-correlation coefficients with MC01 signal being the reference one, textbook outputs stated in lower part of fig. 4.8 are obtained. Both suggest signal periodicity near  $12 \cdot 10^{-3}$  ms, corresponding to 83.33 kHz. Note that by lower

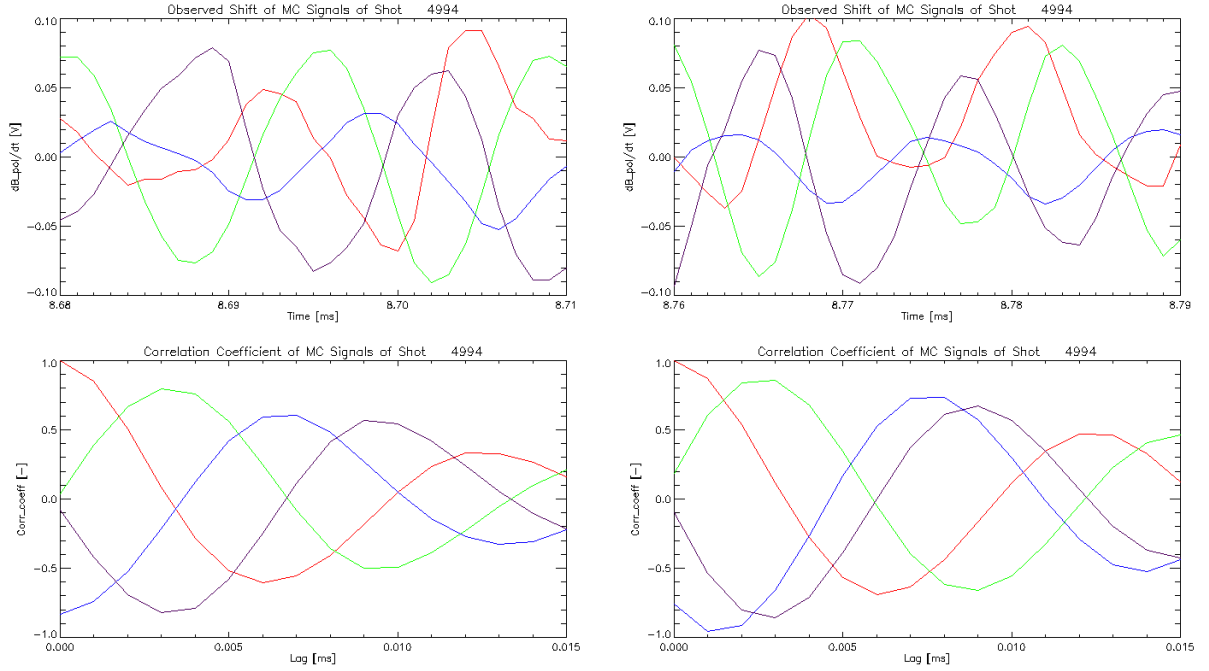


Figure 4.8: High sampling rate comparison of MC signals during initial current rise instabilities of shot 4994 (above), and their resultant correlation coefficients (calculated across the whole depicted evolution) with respect to MC01 (below). Red – MC01, green – MC05, blue – MC09, purple – MC13.

sampling rate DAS, these phenomena could not be detected as its  $f_{Nyquist} = 50$  kHz. By assumption of single event perturbation, this would yield poloidal plasma edge rotation of 31.42 km/s. However observed fluctuations are most likely in form of magnetic islands of higher  $m$  values. Since there are not enough MC sensors yet (not to mention that even with them are high  $m$  islands hard to identify),  $m$  has to be estimated from global parameters by eq. 2.33. This yields  $q(a_2) \approx 5$ , meaning that resultant island rotation would be 6.28 km/s (corresponding to frequency of 16.67 kHz). These values seem to better agree with rotation of range 1.5 - 10 km/s observed on TM-2 tokamak in ref. [22], not to mention that observed order of rotation corresponds to CASTOR experience as well.

# Chapter 5

## Summary

In this paper, MHD activity of GOLEM plasma under different operation regimes was investigated. For these purposes, an introduction into theory of basic MHD instabilities had to be provided first. Manifestation of these instabilities is primarily in form of magnetic islands, which can be characterised by their  $m/n$  ratio, width and characteristic growth time. Estimations of these quantities, with dependence on global plasma parameters are given by relations 2.33, 2.9 and 2.40 respectively. Ref. [4] contains analysis on problematics of emergence of MHD instabilities with respect to plasma  $\sigma$  parameter and on conditions of growth and saturation of their dimensions. Ref. [2] characterises three types of disruptive MHD instabilities of which only low  $q$  operation and high density ones are relevant for tokamak GOLEM.

In section on current GOLEM chamber condition is this tokamak associated rather with Alcator A and T-3 tokamaks than with more recent devices. It is also stated that vacuum pressures are of an order higher than on tokamak CASTOR. Further comparison of basic discharge parameters of these tokamaks yields that standard discharge and plasma parameters of tokamak GOLEM are halved with respect to the ones of CASTOR. The resulting  $q$  profile values are thus expected to be approximately twice as high as those of CASTOR, which limits MHD analysis to higher  $m$  islands. Report also presents models of generated magnetic field components, based on Biot-Savart's law (which is equivalent to Ampere's law). Correspondence of these models to directly measured magnitudes of generated field component yields thumb rules: passive stabilisation vertical component (see fig. 3.6) yields  $B_V$  [T] =  $4.20 \cdot 10^{-6} \cdot I_{coil}$  [A], central toroidal component  $B_T$  [T] =  $1.09 \cdot 10^{-4} \cdot I_{coil}$  [A], plasma edge poloidal component  $B_\theta(a_1)$  [T] =  $2.35 \cdot 10^{-6} \cdot I_p$  [A] (for standard limiter) and  $B_\theta(a_2)$  [T] =  $3.33 \cdot 10^{-6} \cdot I_p$  [A] (for small limiter) with  $I_{coil}$  representing current flowing in respective windings and  $I_p$  total plasma current. Overall

thumb rule for all three components of magnetic fields of tokamak GOLEM:  $B_T \sim (5 \cdot) 10^2$  mT,  $B_\theta \sim 10^1$  mT and  $B_r \sim 10^0$  mT (the last component magnitude taken from ref. [19]). Investigation into validity of  $1/R$  decrement  $B_T$  profile with respect to models and measurement is contained in this section as well, with results that as far as limiter radius is concerned, no toroidal field ripple is expected from models, although it is detected by magnetic sensor to very small degree. Characterisation of currently available magnetic diagnostics means of tokamak GOLEM (containing calibration of sensors in question) suggest necessity of their enrichment. This is carried out by development of new set of local  $\mathbf{B}$  sensors placed around poloidal circumference on newly constructed support structure. This set consists of 16 new MCs and experimental 3D extended temperature Hall sensors developed with collaboration of University of Poznan.

Poloidal mode numbers  $m$  of expected magnetic islands at the plasma edge are given by  $q$  profiles (under assumption of  $\nu = 2$ ) in fig. 4.1. Application of relation 2.9 yields unexpectedly large island dimensions with respect to ref. [4], it is thus concluded that this estimative relation is applicable only on small  $m$  islands. Application of eq. 2.40 on old CASTOR data yields  $\tau_g \approx 1$  ms for 40 ms long discharges.

Analysis of GOLEM database by global discharge parameters and statistical methods of Fourier transformation and cross-correlation has shown several new characteristics of plasma behavior. Without presence of stabilising  $B_V$  field, plasma edge behavior indicates drift of plasma column towards LFS and top of the chamber. Upon application of this field, fluctuations observed by MC01 coil located on LFS start to mitigate, while growing on HFS, as observed by MC09. As for MC05 located on the top side, fluctuations observed seem to be invariant on  $B_V$  presence as it does not influence vertical plasma column position. It is therefore strongly recommended to carry out similar analysis with presence of an additional stabilising  $B_H$  field of horizontal orientation, in order to exploit possibilities of improvement in plasma confinement on this tokamak.

Correlation analysis carried out on fast DAS sampling rate obtained during small limiter session reveals presence of Mirnov instabilities across initial plasma current rise. Results in fig. 4.8 are straightforward to interpret as a poloidal rotation of magnetic field structures with frequency of 83.33 kHz. By identification of these structures as magnetic islands at plasma edge (with  $m$  corresponding to 5, given by global parameters), this would yield plasma edge rotation velocity to be of 6.28 km/s (or 31.42 km/s assuming the less likely single event fluctuation scenario). Observed orders of rotation correspond both to TM-2 tokamak and CASTOR tokamak orders.

# References

- [1] P.C. de Vries, et al, "Survey of disruption causes at JET," *Nucl. Fusion*, vol. 51, 2011.
- [2] J.A. Wesson, et al, "Disruptions in JET," *Nucl. Fusion*, vol. 29, 1989.
- [3] R. Fitzpatrick, "Helical Temperature Perturbations Associated with Tearing Modes in Tokamak Plasmas," *IFSR no. 663 Research Report for Institute for Fusion Studies*, The University of Texas at Austin, 1994.
- [4] J.A. Wesson, *Tokamaks*, Clarendon Press, Oxford, 2004.
- [5] P. Kulhánek, *Úvod do teorie plazmatu* [Introduction to theory of plasma], Aldebaran Group for Astrophysics, Prague, 2011.
- [6] R.S. Granetz, I.H. Hutchinson, D.O. Overskei, "Disruptive MHD Activity During Plasma Current Rise in Alcator A Tokamak," *Nucl. Fusion*, vol. 19, 1979.
- [7] S. M. Weston, *Fusion Plasma Physics*, WILEY-VCH Verlag GmbH & Co. KGaA, Weinheim, 2005.
- [8] T.J.M. Boyd and J.J. Sanderson, *The Physics of Plasmas*, Cambridge University Press, Cambridge, 2003.
- [9] J. Freidberg, *Plasma Physics and Fusion Energy*, Cambridge University Press, Cambridge, 2007.
- [10] S. von Goeler, et al, "Studies of Internal Disruptions and  $m = 1$  Oscillations in Tokamak Discharges with Soft X-Ray Techniques," *Physical Review Letters*, vol. 33, 1974.
- [11] F. M. Levinton, et al, "Stabilisation and Onset of Sawteeth in TFTR," *Physical Review Letters*, vol. 72, 1994.

- [12] H. P. Furth, J. Killeen and M. N. Rosenbluth, "Finite-Resistivity Instabilities of a Sheet Pinch," *Phys. of Fluids*, vol. 6, 1963.
- [13] S. V. Mirnov and I. B. Semenov, "Investigation of the Instabilities of the Plasma String in the Tokamak T-3 by Means of a Correlation Method," *Atomnaya Energiya*, vol. 30, 1971.
- [14] V. Svoboda, et al, "Former Tokamak CASTOR Becomes Remotely Controllable GOLEM at the Czech Technical University in Prague," *37<sup>th</sup> EPS COntference on Plasma Physics*, June, 2010.
- [15] J. Brotánková, "Studium horkého plazmatu v experimentálních zařízeních typu Tokamak" [Study of High Temperature Plasma in Tokamak-like Experimental Devices], doctoral dissertation, Dept. Surface and Plasma Science, Faculty of Mathematics and Physics, Charles Univ. in Prague, 2009.
- [16] M. Valovič, "Magnetic Diagnostics on the CASTOR Tokamak," *Czechoslovak Journal of Physics*, vol. B 38, 1988.
- [17] I. Ďuran, "Fluktuace magnetického pole na tokamaku Castor" [Fluctuations of Magnetic Field on Tokamak CASTOR], doctoral dissertation, Dept. Electronics and Vacuum Physics, Faculty of Mathematics and Physics, Charles Univ. in Prague, 2003.
- [18] T. Markovič, "Konfigurace magnetických polí a jejich měření na tokamaku GOLEM" [Magnetic Field Configurations and Their Measurement on Tokamak GOLEM], bachelor thesis, Dept. Physics, Faculty of Nucl. Sciences and Phys. Engineering, Czech Tech. Univ. in Prague, 2010.
- [19] I. Ďuran, "Fluktuace magnetického pole na tokamaku CASTOR" [Fluctuations of Magnetic in the CASTOR Tokamak], master's thesis, Dept. Nucl. Reactors, Faculty of Nucl. Sciences and Phys. Engineering, Czech Tech. Univ. in Prague, 1997.
- [20] I. H. Hutchinson, *Principles of Plasma Diagnostics*, Cambridge University Press, Cambridge, 2002.
- [21] E.J. Strait, et al, "Magnetic Diagnostics," *Fusion Science and technology*, vol. 53, 2008.
- [22] N. D. Vingradova and K. A. Razumova, *Plasma Phys. and Contr. Nucl. Fusion Research*, vol. 2, 1966, p. 617.

# Contents

<b>1</b>	<b>Introduction</b>	<b>1</b>
<b>2</b>	<b>MHD Instabilities of Tokamaks</b>	<b>2</b>
2.1	Magnetic Islands . . . . .	3
2.2	Disruptive MHD Instabilities . . . . .	5
2.3	Basic MHD Instabilities of Tokamak . . . . .	8
2.3.1	Ideal MHD Instabilities . . . . .	9
2.3.2	Resistive MHD Instabilities . . . . .	17
<b>3</b>	<b>Tokamak GOLEM Characterisation</b>	<b>22</b>
3.1	Discharge Properties and Magnetic Fields of Tokamak GOLEM . . . . .	24
3.2	State and Calibration of Magnetic Diagnostics of Tokamak GOLEM . . .	29
<b>4</b>	<b>MHD Activity of Different Shot Regimes</b>	<b>35</b>
4.1	Calm GOLEM Discharge Without Stabilisation . . . . .	37
4.2	GOLEM Discharge With Stabilisation . . . . .	40
4.3	Unstable GOLEM Discharge with Small Limiter . . . . .	43
<b>5</b>	<b>Summary</b>	<b>46</b>